Present-day interseismic surface deformation along the Longitudinal Valley, eastern Taiwan, from a PS-InSAR analysis of the ERS satellite archives

M. Peyret,[1] S. Dominguez,[1] R. Cattin,[1] J. Champenois,[2] M. Leroy,[1] and A. Zajac[1]

[1]   In Taiwan, about one third of the lithospheric plate convergence between Eurasia and the Philippine Sea plate is accommodated on the eastern coast across the narrow Longitudinal Valley (LV). The Longitudinal Valley Fault (LVF) is the main seismically active fault zone in this region. However, the spatial distribution of ground deformation due to interseismic loading on locked fault segments remains widely unknown. To address this problem, we use a "permanent scatterer" (PS) interferometric synthetic aperture radar (InSAR) approach for processing the ERS satellite archives. The PS mean velocity maps allow accurately mapping and quantifying the ground deformation all along the LV. Assuming that, close to the surface, the fault plane along the central LVF creeping segment dips 55° to the east, we derive a slip vector at the surface of ~25 mm/yr with a mean rake of 70°. In agreement with our PS observations, shallow seismicity indicates a clear change in the fault mechanical behavior of the creeping segment around Fuli town. Finally, we propose a combination of the PS velocity fields for estimating a 3-D map of ground deformation. In the southern part of the LV, the vertical component reveals an uplift of the Coastal Range with respect to the LV of ~10 mm/yr. Moreover, between Taitung and Luyeh, the vertical deformation is essentially accommodated along the Luyeh Strand. Finally, north of Rueisuei, the Coastal Range uniformly subsides at ~15 mm/yr relative to the western side of the LV. However, a local uplift pattern is detected around latitude 23°42′.

1.   Introduction

[2]   The island of Taiwan grows in response to the ongoing oblique collision between the Luzon Volcanic Arc (LVA), carried by the Philippine Sea plate (PSP), and the Eurasian plate (EP). This collision started less than 5 Myr ago and progressively migrates southward [e.g., *Suppe*, 1981; *Ho*, 1986; *Teng*, 1990; *Kao et al.*, 1998; *Lallemand et al.*, 2001; *Bos et al.*, 2003; *Chang et al.*, 2003]. The Taiwan orogen is located at the junction between two subduction systems. To the north, the PSP subducts beneath the southeast facing Ryukyu arc-trench system, while to the south, the South China block subducts beneath the PSP along the west facing Luzon Arc-Manila trench system (Figure 1a). Owing to plate geometry and kinematics, the maturation of the arc-continent collision increases from south to north [e.g., *Huang et al.*, 1997; *Shyu et al.*, 2006b;

Malavieille and Trullenque, 2009], and the suture is exposed subaerially in the Longitudinal Valley (LV) (Figure 1b). This 150 km long NNE trending valley marks the boundary between the Central Range which constitutes the hinterland of the orogen (composed of deformed Eurasian continental margin sediments and metamorphic basement rocks) to the west from the Coastal Range (formed by accreted Luzon Volcanic Arc and forearc sediments units) to the east [e.g., *Ho*, 1986, 1988]. The straight and narrow LV is mainly filled by Quaternary clastic alluvial and fluvial sediments.

[3]   The convergence rate across the whole island is estimated to about 80 mm/yr in N310° direction (Figure 1a) [e.g., *Yu et al.*, 1997; *Hsu et al.*, 2009b]. About 10 mm/yr of shortening is accommodated between the Lutao Island (East) and the eastern coast of the Coastal Range, ~7.5 mm/yr across the Coastal Range, and about one third (25 to 35 mm/yr) of the total convergence is accommodated across the LV [e.g., *Yu and Kuo*, 2001; *Chen et al.*, 2004]. The remainder of the crustal convergence (30 to 40 mm/yr) takes place within the western foothills fold-and-thrust belt. According to *Yu and Kuo* [2001], interseismic shortening rates across the LV slightly decrease from south (34 mm/yr in N314° direction in Taitung) to north (25 mm/yr in south-north

[1]Géosciences Montpellier, Université Montpellier 2, CNRS UMR-5243, Montpellier, France.
[2]Laboratoire Géomatique, Télédétection, Modélisation des connaissances, Université Paris-Est, Marne-la-Vallée, France.
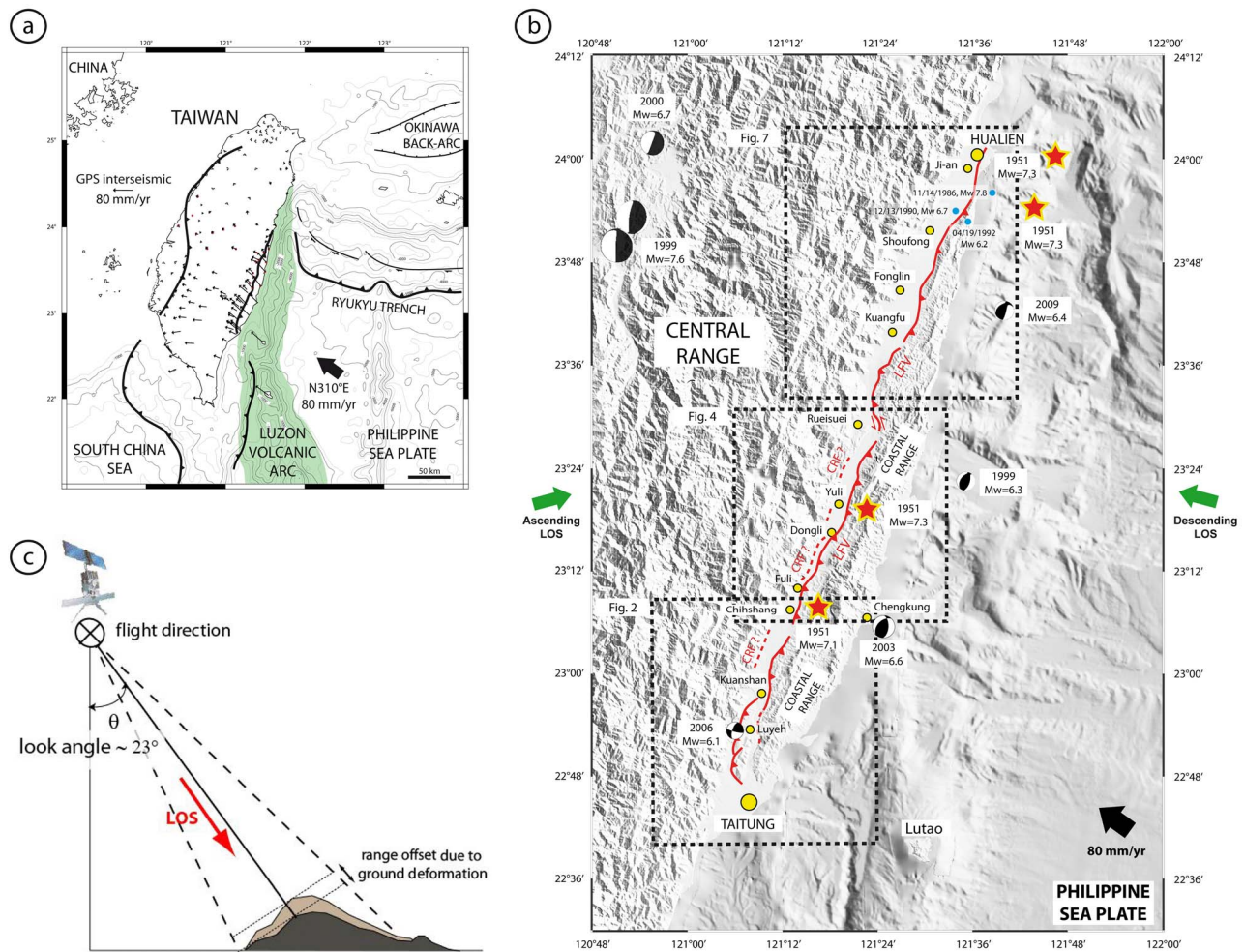
Figure 1. (a) Tectonic context of Taiwan. The island of Taiwan is located at the junction between two subduction systems. To the north, the Philippine Sea plate subducts beneath the Ryukyu arc-trench system, while, to the southwest, the South China block subducts beneath the Philippine Sea plate along the Luzon arc-Manila trench system. (b) Seismotectonic map of the Longitudinal Valley (LV) and Coastal Range (CR). Fault traces are from *Shyu et al.* [2005] and *Yu and Kuo* [2001]. Blue circles stand for earthquakes with magnitude higher than 6 since 1973 that occurred prior the time interval spanned by this study (USGS earthquakes catalog http://earthquake.usgs.gov). No earthquake with magnitude higher than 6 occurred in the vicinity of the LV during this time interval (June 1993 to September 1999). Focal mechanisms are from the Harvard CMT catalog (http://www.globalcmt.org). The convergence rate estimated by GPS between the Philippine Sea plate and Eurasia is 80 mm/yr in northwest direction [*Yu et al.*, 1997]. (c) Simplified geometry of a right-side looking radar system. The radar signal propagates toward the Earth surface along the satellite line of sight (LOS) with a mean look angle of 23° in the case of ERS acquisitions. In case of ground deformation between two acquisitions (schematically depicted with the black and the gray topographies), the radar interferogram will measure the range offset along the LOS. The black dotted lines perpendicular to the LOS represent the radar waves.

direction in Hualien). The maximum compression axis rotates clockwise from N60°W in the Taitung area to N30°W in the Hualien area [*Hsu et al.*, 2009b].

[4] Across the LV, crustal shortening is accommodated essentially by the Longitudinal Valley Fault (LVF) and the Central Range Fault (CRF) which trend parallel to the LV geological boundary. The LVF runs along the eastern side of the LV and is, by far, the major active fault in this region. It corresponds to a high-angle oblique thrust fault with a minor left-lateral strike-slip component [*Barrier et al.*, 1982; *Yu and Liu*, 1989; *Yu and Kuo*, 2001]. On the hanging wall

of the LVF, rapid and stable uplift (about 20 mm/yr) of the Coastal Range has been reported [e.g., *Lee and Angelier*, 1993; *Chen et al.*, 2004]. The fault appears to be weakly locked and mainly characterized by aseismic slip [e.g., *Yu and Kuo*, 2001]. Shallow creeping behavior is prominent especially along a 60 km long segment located between latitudes 23°00′ and 23°30′ [e.g., *Yu and Liu*, 1989; *Angelier et al.*, 1997; *J. C. Lee et al.*, 2001, 2003; *Hsu and Bürgmann*, 2006].

[5] Nowadays, the LVF exhibits different behaviors: some segments slip aseismically with rapid creep, whereas

major earthquakes have occurred on other segments. In 1951 the LVF generated several M > 7 earthquakes associated to long coseismic surface ruptures (Figure 1b) [e.g., *Cheng et al.*, 1996; *Shyu et al.*, 2007; *Chung et al.*, 2008]. More recently, the fault partly ruptured during the 2003 Chengkung Mw = 6.6 earthquake [e.g., *Chen et al.*, 2006; *Wu et al.*, 2006; *Cheng et al.*, 2009; *Hsu et al.*, 2009a; *Mozziconacci et al.*, 2009] and also during several other moderate earthquakes close to Hualien in 1986 [e.g., *Liu and Yu*, 1990; *Kao and Jian*, 2001; *Kuochen et al.*, 2004; *Wu et al.*, 2007, 2008].

[6] The Central Range Fault (CRF) follows the eastern flank of the Central Range, mostly in the southern two thirds of the valley. The CRF slips at a lower rate (about one half) than the LVF [*Shyu et al.*, 2006a, 2008]. Various interpretations of this fault behavior have been published [e.g., *Crespi et al.*, 1996; *J. C. Lee et al.*, 2001, 2003; *Malavieille et al.*, 2002]. Yet, there is abundant evidence that it is reverse west dipping, at least at shallow depths [*Shyu et al.*, 2006b; *Wu et al.*, 2006].

[7] To better constrain active deformation distribution along the LV and Coastal Range, surface fault geometries and present-day kinematics, dense measurements of ground deformation are needed. With this aim, a special effort has been made for developing a dense GPS network all over the LV. However, this point-wise technique cannot provide an adequately dense mapping of the deformation affecting the LV.

[8] Radar interferometry (InSAR) technique theoretically is able to reach decametric resolution with subcentimeter precision in the surface displacements measurements. However, despite the published work of *Hsu and Bürgmann* [2006], heavy temporal decorrelation on the interferometric signal due to steep slopes on the mountain belts, high vegetation coverage within the valley, and highly variable weather conditions, seriously limits the efficiency of this approach in the LV area.

[9] The "permanent scatterers" or "persistent scatterers" interferometric synthetic aperture radar (PS-InSAR) technique allows partially overcoming these limitations [*Ferretti et al.*, 1999, 2001]. Here we present the results of this approach applied to the ERS satellite archives from 1993 to 1999 acquired prior to the Chi-Chi earthquake (27 September 1999, Mw 7.6). Over this time period, no major earthquake occurred along the LV. Thus, in the following, we consider that ground deformation is related to interseismic deformation only and can be compared to the available interseismic GPS velocity fields [*Hsu et al.*, 2009b; *Huang et al.*, 2010]. After reviewing the basics of the PS-InSAR approach, we will illustrate in detail the velocity maps derived from the PS-InSAR analysis. These velocity fields are then combined with GPS constraints to produce a reliable interseismic 3-D velocity map across the LV and the east central coast of Taiwan. Finally, we derive the surface slip vector on the fault plane along the creeping segment in the middle of the LVF from the measured PS velocity gradients across the fault.

2. Methodology of PS-InSAR and Data Set

[10] Mapping heterogeneous ground deformation patterns, especially near-fault deformation, requires measurements at a spatial density that cannot be easily achieved by point-based techniques like levelling or GPS. Moreover, the measurement of the vertical component of displacement by GPS is much less constrained than the horizontal (centimeter precision compared to millimeter). For these reasons, radar interferometry (InSAR) [e.g., *Massonnet and Feigl*, 1998; *Bürgmann et al.*, 2000] is the most efficient technique to complement GPS measurements. Theoretically, it provides spatially dense (decameter-scale) measurements of ground displacement with subcentimeter precision. However, InSAR is only sensitive to ground displacement along the satellite line of sight (LOS) (Figure 1c). The LOS in the descending pass is roughly perpendicular to the faults of the LV and consequently almost completely insensitive to any fault-parallel displacement, whereas this motion will be partly detected in the ascending pass (Figure 1b).

[11] In practice, InSAR requires the conservation of geometrical and physical properties of homologous pixels between a pair of satellite acquisitions [*Zebker and Villasenor*, 1992]. For radar systems using electromagnetic waves in the C band range (wavelength 5.6 cm), the main source of decorrelation is related to vegetation coverage.

[12] The second main limitation to ground deformation analysis by InSAR is the interferometric phase delay due to relative changes in atmospheric conditions (from the troposphere and the ionosphere) between two acquisitions [e.g., *Zebker et al.*, 1997]. This effect adds spatially coherent noise on phase at spatial scales ranging from several hundred meters to tens of kilometers. The typical amplitude of these artifacts is about one fringe (equivalent to a 2.8 cm range change between ground and satellite in C band). The consequence is that it often becomes challenging to detect small distributed ground deformation gradients (typically 10^{-3} fringe/km for interseismic elastic deformation) simply by a cross analysis of one set of interferograms.

[13] The LV is particularly prone to both of these limitations. Therefore, only one single study of the interseismic strain distribution along the LV by standard InSAR approach has been published [*Hsu and Bürgmann*, 2006]. This study is limited to simply stacking a small subset of independent interferograms in descending orbits. This allowed Hsu and Bürgmann to locate the creeping segment of the LVF and quantify its motion. Nevertheless, phase decorrelation is still important and atmospherical residues are probably still too high for inferring anything dealing with some diffuse ground deformation. Consequently, in the case of the LV, to determine precisely the deformation component of the interferometric phase, even in decorrelated areas, implementation of a more sophisticated approach to interferometric phase analysis, called the "permanent scatterers" or "persistent scatterers" InSAR (PS-InSAR) is required.

[14] The PS-InSAR principle has been originally defined by *Ferretti et al.* [1999, 2001]. It considers the fact that, within spatially decorrelated areas, pixels may exhibit some phase stability over a time series of interferograms. For such pixels, called "permanent" or "persistent" scatterers (PS), one individual scatterer generally dominates the echo. Hence, PS pixels behave like point scatterers and decorrelation is greatly reduced.

[15] Different criteria may be defined for identifying PS pixels in a series of interferograms. The amplitude dispersion index and the signal-to-clutter ratio have been widely

Table 1. List of the ERS Radar Image Processed in the Descending Pass on the Southern Part of the LV[a]

Date	Bperp (m)
23 Jun 1993	224
6 Oct 1993	−121
16 Jun 1995	−12
21 Jul 1995	262
25 Aug 1995	−29
9 Dec 1995	277
12 Jan 1996	97
10 Aug 1996	−79
14 Sep 1996	0
28 Dec 1996	84
1 Feb 1997	315
17 May 1997	167
26 Jul 1997	124
13 Dec 1997	−357
17 Jan 1998	−230
28 Mar 1998	61
2 May 1998	187
11 Jul 1998	−301
15 Aug 1998	107
24 Oct 1998	−180
13 Mar 1999	272
22 May 1999	−166
31 Jul 1999	327
4 Sep 1999	−191

[a]The corresponding perpendicular baselines (Bperp) relative to the master image (14 September 1996) are provided.

Table 3. List of the ERS Radar Image Processed in the Descending Pass on the Northern Part of the LV[a]

Date	Bperp (m)
23 Jun 1993	218
6 Oct 1993	−109
16 Jun 1995	−12
25 Aug 1995	−30
9 Dec 1995	277
12 Jan 1996	107
10 Aug 1996	−69
14 Sep 1996	0
28 Dec 1996	84
17 May 1997	167
26 Jul 1997	130
13 Dec 1997	−365
17 Jan 1998	−226
28 Mar 1998	65
2 May 1998	199
11 Jul 1998	−306
15 Aug 1998	107
24 Oct 1998	−167
13 Mar 1999	264
22 May 1999	−157
31 Jul 1999	339
4 Sep 1999	−197

[a]The corresponding perpendicular baselines (Bperp) relative to the master image (14 September 1996) are provided.

used [e.g., *Ferretti et al.*, 2001; *Adam et al.*, 2004]. They are good proxies for phase standard deviation, but solely for high signal-to-noise ratio. Thus many PS-InSAR analyses are mainly restricted to man-made structures or urban areas.

[16] Furthermore, many PS-InSAR algorithms consider not only that a PS pixel is characterized by a certain phase stability over time, but that its phase history must match an assumed model of how displacement varies with time [e.g., *Ferretti et al.*, 1999, 2001; *Lyons and Sandwell*, 2003; *Werner et al.*, 2003; *Adam et al.*, 2004; *Kampes*, 2005]. Commonly, deformation is assumed to be steady state although no limitation exists to the complexity of this a priori model. Only a pixel whose phase history is similar to the assumed model of deformation is deemed valid. However, if some PS can be identified, deviations from the parametric model may be estimated from the residuals [*Ferretti et al.*, 2000; *Colesanti et al.*, 2003; *Kampes*, 2005].

[17] Once a PS data set has been determined, the PS-InSAR processing can focus on the analysis of the phase time

Table 2. List of the ERS Radar Image Processed in the Ascending Pass on the Southern Part of the LV[a]

Date	Bperp (m)
30 Oct 1993	−40
4 Dec 1993	318
1 May 1995	162
5 Jun 1995	−284
27 Nov 1995	235
1 Jan 1996	−296
2 Jan 1996	0
11 Mar 1996	134
12 Mar 1996	369
21 May 1996	37
25 Jun 1996	151

[a]The corresponding perpendicular baselines (Bperp) relative to the master image (2 January 1996) are provided.

series for each PS. This involves removing the residual topographic component of the flattened interferogram phase and then unwrapping the PS phase both spatially and temporally. This analysis enables one to isolate the deformation signal, including a step in which most of the atmospheric signal is estimated and removed by considering that it is correlated spatially and uncorrelated temporally [e.g., *Ferretti et al.*, 2001].

[18] In this study, we use the Stanford Method for Persistent Scatterers (StaMPS) method [*Hooper*, 2006; *Hooper et al.*, 2004, 2007]. Contrary to most PS selection strategies, StaMPS uses spatial correlation of phase measurements to identify PS pixels [e.g., *Hooper et al.*, 2004; *Van der Kooij et al.*, 2005]. The probability for a pixel to be a PS is estimated through phase analysis, which is successively refined in a series of iterations. This strategy allows the detection of PS pixels even though their amplitude is low, which is often the case in natural terrains, and without any prior assumption about the temporal nature of ground deformation. Instead of requiring a known temporal dependence of deformation, StaMPS simply leans on the spatially correlated nature of the deformation.

[19] In the following, we present the results of the PS-InSAR analysis of the ERS SAR archives acquired from 1993 to 1999 along the eastern coast of Taiwan using both the ascending and the descending pass (Tables 1 to 4). The differential interferograms have been constructed with "Roi_pac" [*Rosen et al.*, 2004] and "Doris" software. We used precise ERS orbits from Delft [*Kampes et al.*, 2003]. We flattened and georeferenced the interferograms using the TWD67 digital elevation model (40 m resolution).

3. Result: Mean Velocity Fields Estimated by PS-InSAR

[20] All the image time series are processed using a wide range of thresholds related to the probability for a selected

Table 4. List of the ERS Radar Image Processed in the Ascending Pass on the Northern Part of the LV[a]

Date	Bperp (m)
30 Oct 1993	−39
4 Dec 1993	325
1 May 1995	152
5 Jun 1995	−285
27 Nov 1995	226
2 Jan 1996	0
11 Mar 1996	139
12 Mar 1996	368
21 May 1996	34
25 Jun 1996	145
2 Nov 1999	−129

[a]The corresponding perpendicular baselines (Bperp) relative to the master image (2 January 1996) are provided. The 2 November 1999 event indicates an image acquired after the Chi-Chi earthquake. The PS velocity maps presented in the paper only use data acquired before this event. Nevertheless, in order to significantly increase the time interval spanned by the ascending acquisitions, we also processed this data set including this recent image. The mean velocity results are totally similar.

pixel to be a false PS. The higher the threshold, the denser are the PS maps, but the probability of including unreliable information increases. Beyond a certain threshold, the PS mean velocity fields partly cease to conform to the ones obtained with lower thresholds. Therefore, among the various thresholds tested, we selected the highest one that guarantees the similarity of all the mean velocity fields obtained for lower thresholds. Even though such a selection should be, in principle, spatially variable, we simply chose a unique threshold for the whole scene. So, the PS mean velocity fields that we present in this study should include no more than ~10% of false PS. The counterpart of this strict selection is that the spatial density of PS is rather small (a few tens of PS per kilometer squared) or even quasi-null within the Central and Coastal Ranges.

[21] Over the whole LV in both the ascending and the descending pass, the spatial distribution of the temporal standard deviation of the radar phase with respect to the mean velocity estimated by StaMPS is uniform. It is estimated to about 2 mm/yr (±1 mm/yr). We detected only one significant exception that will be discussed in section 3.2. This attests to both the accuracy of the PS velocity estimates and the global validity of the constant deformation model implicitly used when considering solely the mean velocity over the studied time series.

[22] In section 3 a spatial linear trend has been removed from each velocity field. The objective is simply to remove any constant velocity gradient across the LV in order to better highlight the main features of local deformation.

3.1. South LV: From Taitung (Latitude 22°45′) to Kuanshan (Latitude 23°)

[23] The Taitung plain (TP) marks the southern edge of the LV and the Coastal Range. It constitutes also the transition zone between deformation associated to the continental subduction to the north and the one related to the oceanic subduction to the south. It is generally acknowledged that in its southern part, the LVF splits into the Luyeh Strand (LS) to the west and the Peinan Strand (PeS) to the east and ends along the southern extremities of the Peinanshan Terraces and the Coastal Range [e.g., *Shyu et al.*, 2008].

[24] The PS mean velocity maps (Figure 2) reveal a diffuse ground deformation all over the TP. However, some significant changes in the velocity gradients can be observed along the eastern flank of the Central Range (profiles P1-P2 in Figure 2). Their amplitude is ~5 mm/yr in both LOS, though slightly lower in the descending pass for P1. Indeed, the linear trend observed on the eastern part of the TP is disturbed about 2 km from the foot of the CR. This could be related to the elastic deformation centered on a fault segment running along the CR and whose locking depth would be as shallow as 1 or 2 km. Unfortunately, the lack of reliable PS measurements within the CR prevents the confirmation of this interpretation. We believe that PS on the western side of this fault segment should exhibit the roughly symmetric part of this elastic ground deformation. However, it is noticeable that no morphological evidence of fault activity has been reported in this area up to now. The CRF becomes apparent only farther to the north [*Shyu et al.*, 2006b]. However, this present-day deformation mapped by PS-InSAR probably corresponds to a blind southward propagation of the CRF that would accommodate the eastward back thrust motion of the CR.

[25] When reaching the southern flank of the Peinanshan terraces (PT), two PS mean velocity profiles (P3-P4 in Figure 2) reveal a clear change in south-north velocity gradient. Significant surface deformation is clearly localized at the foot of this relief, in the prolongation of the Luyeh Strand, indicating that this fault zone is still active when wrapping eastward around the southern PT. This activity is discernable all along the southern tip of the Coastal Range. Then, this segment probably connects offshore with the reverse faults and back thrusts trending N-S that affect the Huatung ridge and the Taitung trough [*Malavieille et al.*, 2002; *Malavieille and Trullenque*, 2009].

[26] The shape of the PS profiles radically changes at the latitude of the Peinanshan terraces (Figure 3). These terraces (likewise the Kaotai terraces farther north) correspond to alluvial surfaces uplifted above a popup structure associated with the activity of the Luyeh Strand (LS) and the Peinan

Figure 2. PS velocity map in the (top left) descending pass and the (top right) ascending pass at the southern extremity of the LV, across the Taitung plain (TP). The white lines indicate the location of the profiles that are shown below (P1 to P4). PS velocity profiles are superimposed on the topographic profiles from the TWD67 40 m resolution digital elevation model. Black dotted lines show the location of significant gradient changes in the PS velocity maps. They are all in agreement with the fault traces (LS, Luyeh Strand; PeS, Peinan Strand) estimated from geological and geomorphologic field surveys [e.g., *Yu et al.*, 1997; *Shyu et al.*, 2006b, 2008]. The velocity gradients exhibit a significant change both along the eastern flank of the Central Range (P1 and P2) and at the southern foot of the Peinanshan Terraces (PT) and Coastal Range (P3 and P4). This proves the location and the activity of one blind segment along the CR and the Luyeh Strand in this area.
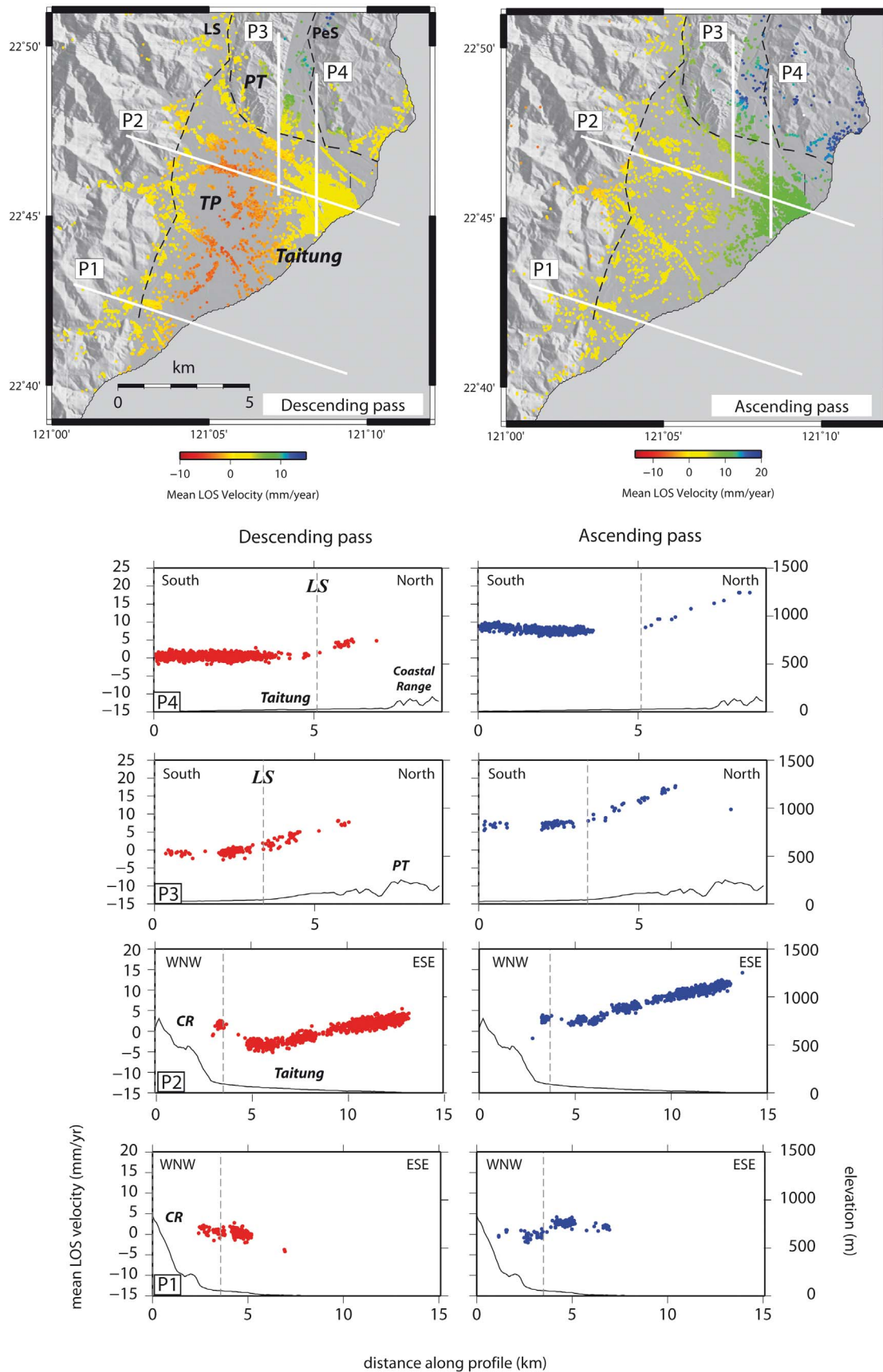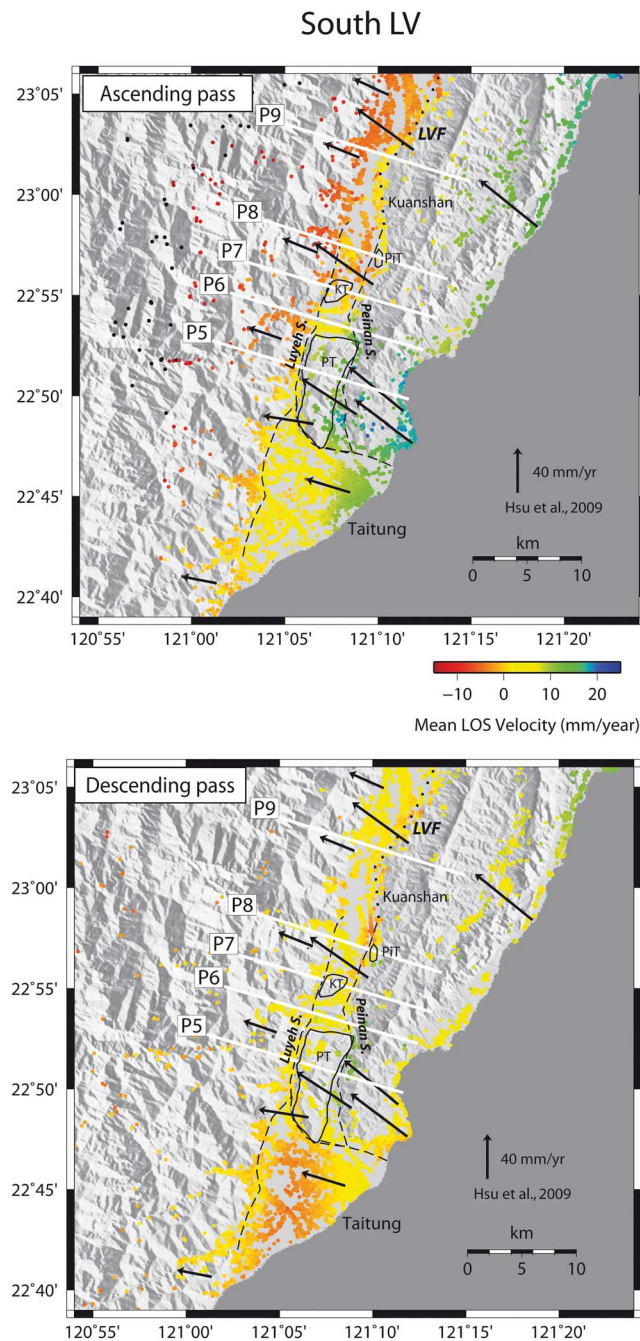
Figure 2

Figure 3. PS mean velocity map in (top) the ascending pass and (bottom) the descending pass between the Taitung plain and Kuanshan. GPS velocity field is from *Hsu et al.* [2009b]. Black dotted lines show the location of significant gradient changes in the PS velocity maps. They are all in agreement with the fault traces estimated from geological and geomorphologic field surveys [e.g., *Yu et al.*, 1997; *Shyu et al.*, 2006b, 2008]. White lines show the location of the profiles presented in the Figure 4. PT, Peinanshan Terraces; KT, Kaotai Terraces; PiT, Pingting Terraces; and LVF, the Longitudinal Valley Fault.

Strand (PeS) fault zone [*Chen et al.*, 2004]. Indeed, the PS velocity profiles (profile P5 in Figure 4) indicate that the gradients of motion across the LV are here clearly located on the LS and the PeS. However, since the LS and the CRF are very close to each other, it is not possible to distinguish their individual contributions to ground deformation. Nevertheless, profiles farther north (e.g., P6 in the Luyeh valley) solve this ambiguity by clearly mapping a steep velocity gradient onto the LS trace while no activity is detected along the CRF trace. In the east-west oriented Luyeh river valley that separates the Peinanshan terraces (south) from the Kaotai terraces (north), the PS velocity fields clearly highlight the location and the activity of the LS southwest of the Kaotai terraces (profile P6 in Figure 4). The gradient of deformation across the LS is very steep both in the two LOS, with an amplitude of ~5 mm/yr. A similar observation can be found across the PeS but with a smaller amplitude. This similarity between the two LOS suggests a predominant vertical motion. Hence, at P6, PeS and LS should be considered there as mainly pure thrusts, and the vertical uplift can be estimated to about 7 and 4 mm/yr on the LS and PeS, respectively. These measurements are in agreement with *Shyu et al.* [2008], who report field evidence of the LS nearby the Lungtien village (southwest of the Kaotai terraces). Moreover, although they consider the LS as a blind reverse fault, they report a few surface breaks close to the Chulu village in the Luyeh valley. Finally, they estimate the relative uplift across the Luyeh fault to more than 4.5 mm/yr, while some leveling data in the Luyeh area indicate as much as 7 mm/yr [*Chen et al.*, 2004]. All of these observations and quantification are in good agreement with the PS velocity maps.

[27] From the north of the Peinanshan terraces to the north of the Kaotai terraces, the gradients of deformation on both LS and PeS are very well localized (P7 in Figure 4). The PS velocity fields clearly indicate that the LS runs between the Kaotai terraces and the Central Range, while the PeS runs within the Luyeh river bed. This latter observation is in agreement with the location of the PeS close to the Luanshan bridge (southwest of Luyeh village) and the Paohua bridge (northeast of Rueiyuan) as reported by *Shyu et al.* [2008] after the Chengkung earthquake.

[28] Finally, surface deformation associated with the LS seems to end about 2 km north of the Kaotai terraces (between profiles P8 and P9 in Figure 4). This result is in agreement with geomorphological observations [*Shyu et al.*, 2008] and GPS measurements [e.g., *Chen et al.*, 2004]. This area is a transition zone between the north where deformation is essentially accommodated by the LVF along the eastern edge of the LV and the south where the LS and the PeS are clearly active on both sides of the LV. No significant PS velocities gradient is detectable on the western part of the LV, north of latitude 23°00′. This suggests that the CRF is inactive (or does not exist) north of 23°00′, whereas, to the south, in the PS velocity fields, its activity may be obscured by that of the LS because of their proximity. On the eastern part of the valley, the PS analysis indicates that the PeS runs west of the Pingting terraces, once again in agreement with geomorphological observations [*Shyu et al.*, 2008]. From this point and northward, the deformation is localized on the eastern side of the LV and distributed over slightly more than 1 km across the PeS (profile P9 in
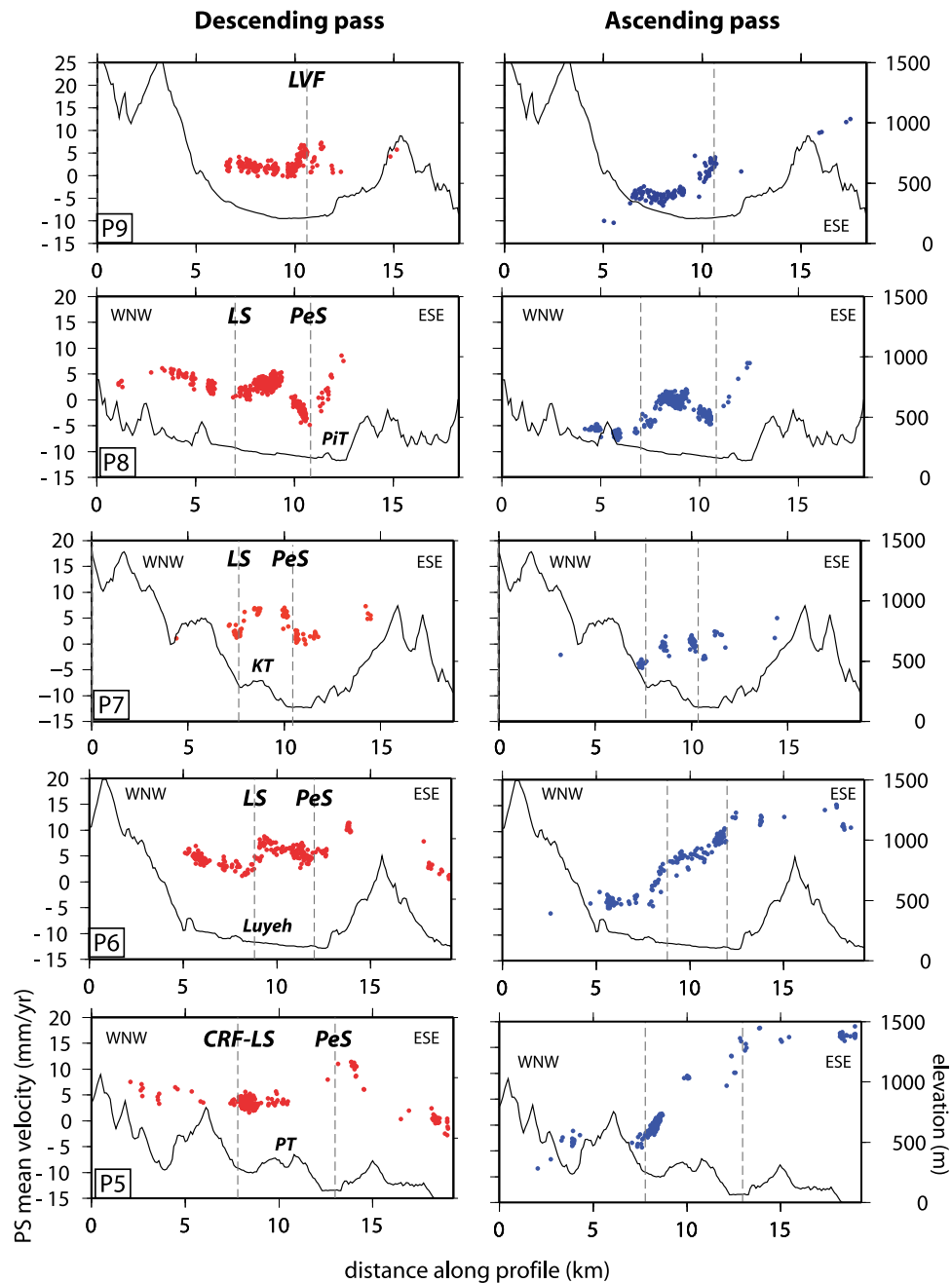
Figure 4. Profiles of PS mean velocities between the Taitung plain and Kuanshan in (left) the descending pass and (right) the ascending pass, superimposed on the topographic profile from the TWD67 40 m resolution digital elevation model. The locations of these profiles are shown in Figure 3. Black dotted lines indicate the likely location of the faults as estimated from the PS velocity maps. They are all in agreement with the fault traces estimated from geological and geomorphologic field surveys [e.g., *Yu et al.*, 1997; *Shyu et al.*, 2006b, 2008]. CRF, Central Range Fault; LS, Luyeh Strand; PeS, Peinan Strand; PT, Peinanshan Terraces; KT, Kaotai Terraces; and PiT, Pingting Terraces.
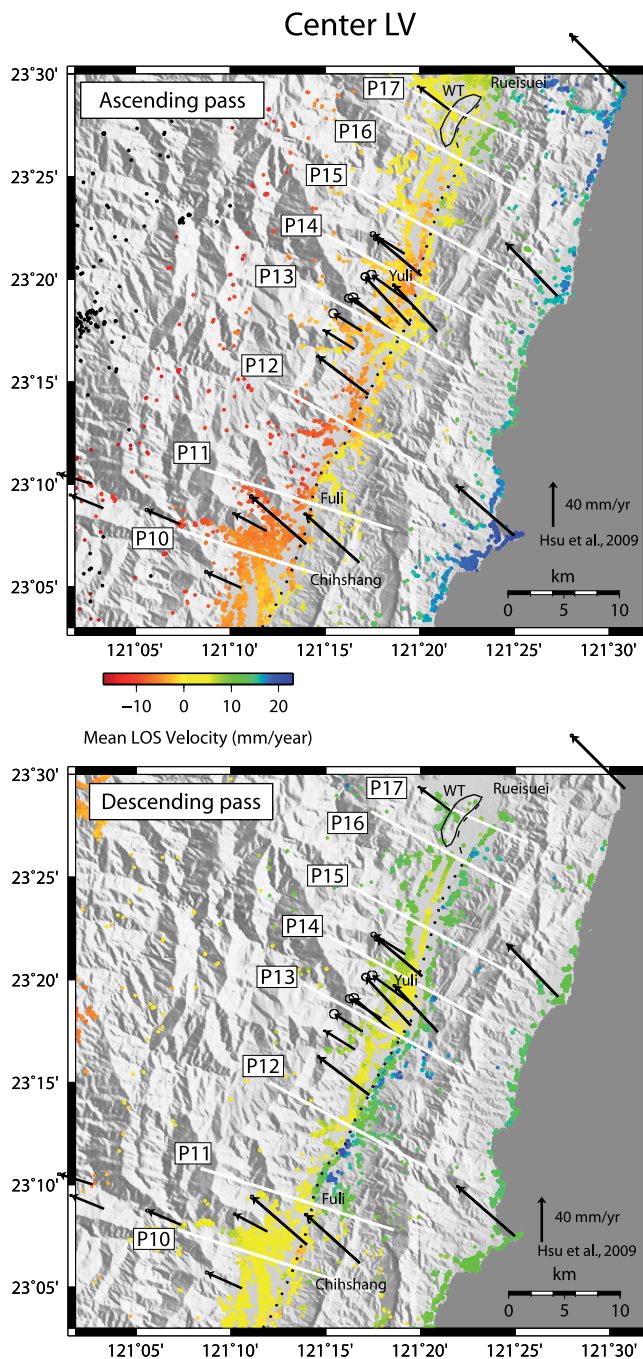
Figure 5. PS mean velocity map in (top) the ascending pass and (bottom) the descending pass between Chihshang and Rueisuei. GPS velocity field is from *Hsu et al.* [2009b]. Black dotted lines show the location of significant gradient changes in the PS velocity maps. They are all in agreement with the fault traces estimated from geological and geomorphologic field surveys [e.g., *Yu et al.*, 1997; *Shyu et al.*, 2006b, 2008]. White lines show the location of the profiles presented in the Figures 6 and 7. WT, Wuhe Tableland.

Figure 4) which means that the locking depth is probably very shallow.

[29] Finally, it is worth noting that despite the very low density of PS within the Central Range and the Coastal Range, our results suggest that there is no localized deformation along any other fault within these two mountain belts.

3.2. Middle LV: From Kuanshan (Latitude 23°00′) to Rueisuei (Latitude 23°30′)

[30] Roughly north of the latitude of Luyeh (22°54′), high velocity offsets at the scale of less than about 1 km are measured along the LVF trace (Figure 5). This kinematics becomes even more obvious north of 23°00′ up to 23°30′ where the fault shows very shallow (or even surface) creep (black dotted line in Figure 5).

[31] Between Kuanshan and Chihshang, the deformation evolves progressively from a relatively diffuse elastic distribution (profiles P8-P9 in Figure 4), yet revealing very shallow locking depth, to a clear surface creep characterized by a sharp discontinuity in the PS velocity fields (profiles P10-P16 in Figures 6 and 7).

[32] Near Chihshang, the PS velocity field in the ascending pass shows a discontinuity as high as about 10 mm/yr along the LVF trace (profile P10). A similar discontinuity exists in the descending pass with slightly lower amplitude, although this latter is rather difficult to quantify due to the scarcity and the dispersion of the PS on the hanging wall. Throughout the Chihshang village northward to Fuli, the pattern of strain distribution in geometry of acquisition remains similar. However, in Fuli (profile P11) the descending pass exhibits a clear discontinuity of about 10 mm/yr that was not detectable with such an amplitude farther south.

[33] The profiles located between Kuanshan and Rueisuei reveal that over the studied time period (1993–1999), only one major fault branch was active. This agrees with field observations indicating that the surface rupture is concentrated within a 30–100 m wide narrow deformation zone [e.g., *Angelier et al.*, 1997]. Moreover, there is no evidence of large-scale gradient changes that could be attributed to any additional elastic distribution. Finally, no significant velocity gradient change occurs along the alluvial fan (between P10 and P11) that stands face to the Coastal Range and creates a local intrusion within the eastern flank of the Central Range. Despite the scarcity of PS in this area, the CRF appears to be inactive at this latitude.

[34] North of Fuli to the north of Yuli, surface creep with discontinuities of ~10 mm/yr in the descending pass is observed. Here, the ascending pass shows that the deformation along its LOS decreases northward to ~0 mm/yr (P12 to P14 in Figures 6 and 7) and then increases again up to ~5 mm/yr (P15 and P16 in Figure 7). This could be related to some fault-parallel creeping motion since the ascending LOS is partly collinear with the fault azimuth, contrary to the descending LOS. On the hanging wall of the LVF (Coastal Range), PS move vertically toward the satellite in both geometries compared with PS located on the footwall. However, this relative motion toward the satellite is partially balanced in ascending pass by a left-lateral motion that makes the PS on the hanging wall moving away from the satellite.
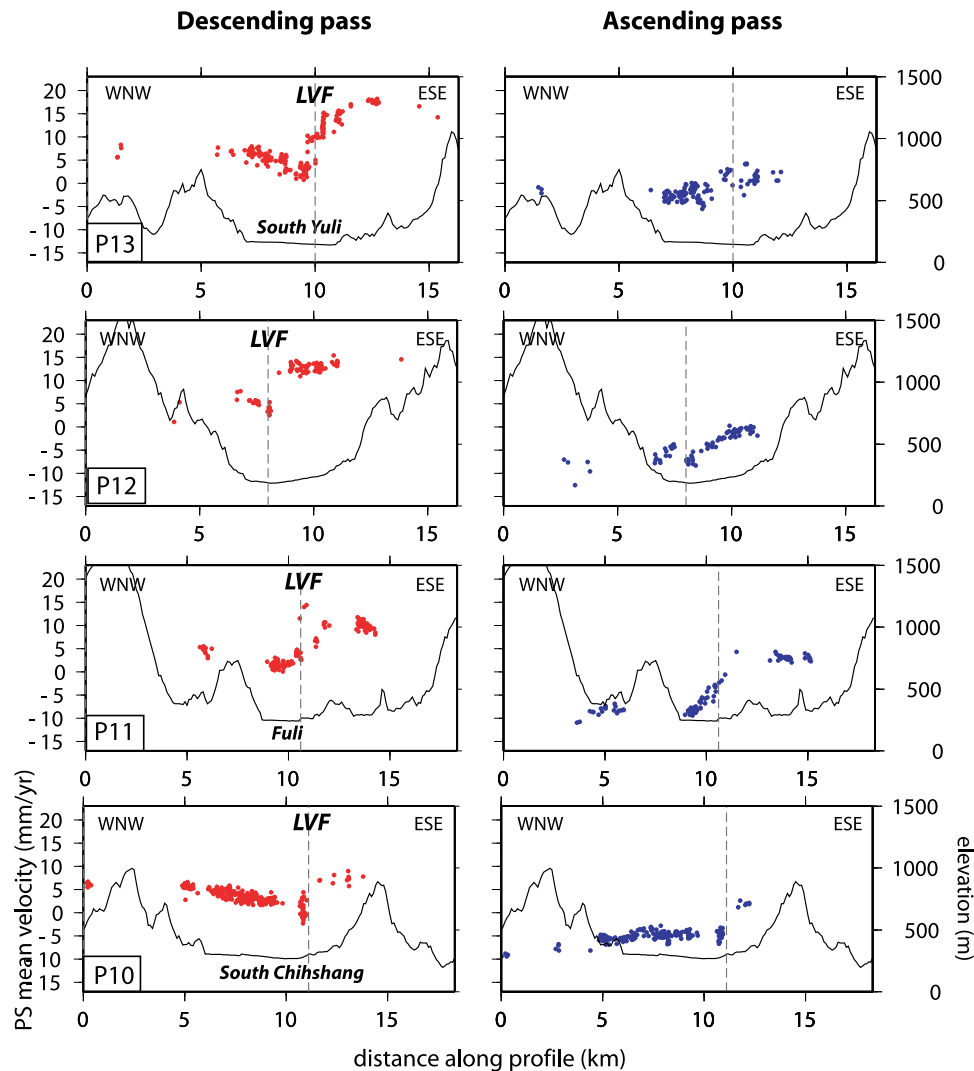
Descending pass **Ascending pass**

Figure 6. Profiles of PS mean velocities between south of Chihshang and south of Yuli in (left) the descending pass and (right) the ascending pass, superimposed on the topographic profile from the TWD67 40 m resolution digital elevation model. The locations of these profiles are shown in Figure 5. Black dotted lines indicate the likely location of the faults as estimated from the PS velocity maps. LVF, Longitudinal Valley Fault.

[35] In this area, several studies indicate that the hanging wall of the LVF in this area experiences uplift over the LV floor by about 13 mm/yr [*Liu and Yu*, 1990; *Yu and Kuo*, 2001]. Projecting this deformation onto the descending LOS (and neglecting to the first-order any horizontal compressive deformation) leads to a predicted PS velocity change of about 12 mm/yr which is very similar to the 10 mm/yr estimated in our analysis.

[36] To illustrate the fine spatial resolution of the PS velocity fields, we present one profile located along the Yuli Bridge (Figure 8). If this example is not the most favorable from a spatial density point of view, it has the advantage of being directly comparable to GPS measurements. Indeed, *Yu and Kuo* [2001] report that the eastern end of the bridge moves horizontally with respect to its western end by 22.8 mm/yr in 306° direction. As expected, the PS profiles indicate that the LVF clearly passes in the riverbed some-

where beneath the Yuli bridge (Figure 8). The exact location is unknown because no PS is available on the bridge itself which is a surprise since most manmade structures provide reliable PS as observed for the numerous linear structures of the river dams (Figure 8). This lack of PS on the bridge remains even when using less restrictive thresholds for the PS selection. This could be explained by some restoration work during the studied time period, but we have not such information. This highlights the complexity of the radar scattering process and the difficulty to predict whether one target will be selected as PS or not, even with apparently steady geometric and physical properties. In contrast, numerous unexpected PS are found within the riverbeds. They likely correspond to large rocks whose scattering properties are well preserved over time.

[37] Finally, it is worth noting that, in the ascending pass, the standard deviation of the radar phase significantly
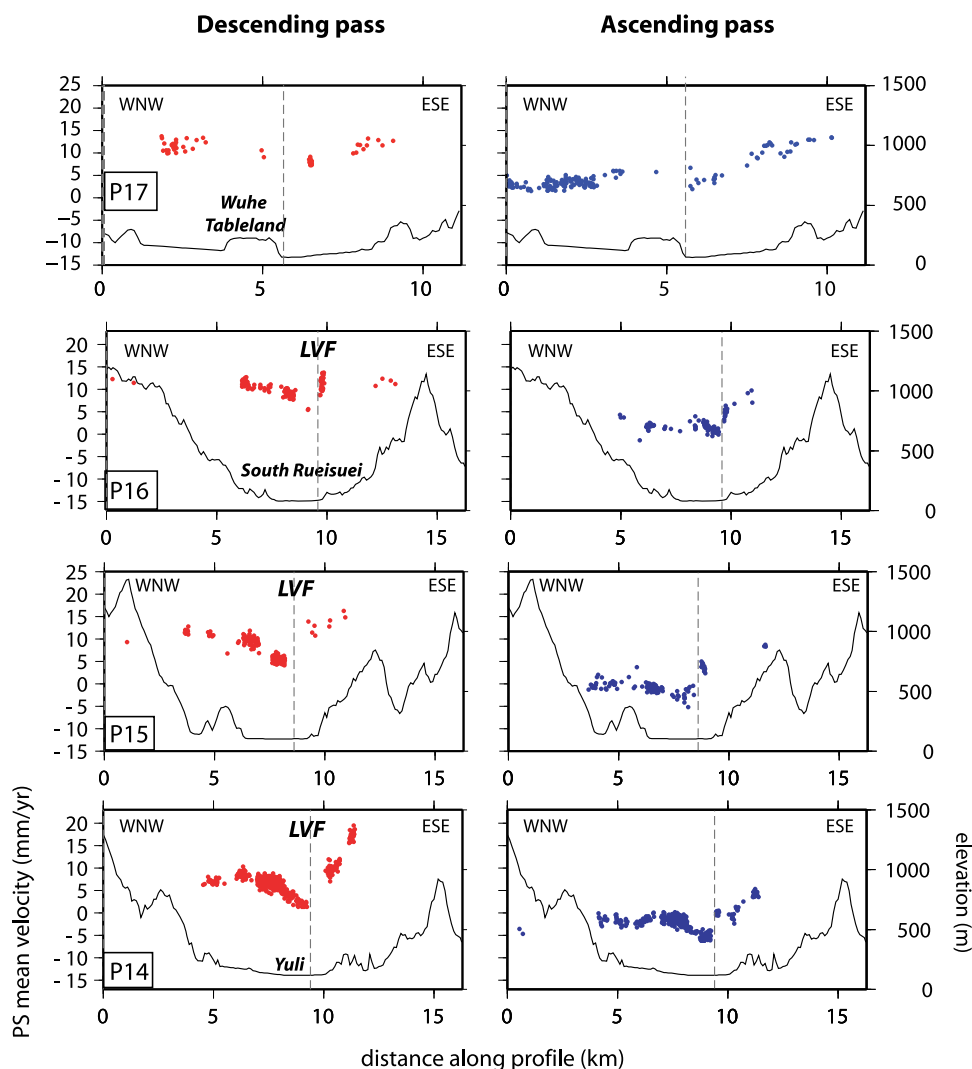
Figure 7. Profiles of PS mean velocities between Yuli and Rueisuei in (left) the descending pass and (right) the ascending pass, superimposed on the topographic profile from the TWD67 40 m resolution digital elevation model. The locations of these profiles are shown in Figure 5. Black dotted lines indicate the likely location of the faults as estimated from the PS velocity maps. LVF, Longitudinal Valley Fault.

increases from ~2 mm/yr (as observed almost everywhere else) to ~4 mm/yr along the eastern side of the creeping segment between latitudes 23°10′ and 23°15′ with some local maxima as high as 6 mm/yr. This effect is not observed in the descending pass. The small number of images in this data set cannot explain this decrease in accuracy since it should affect the whole processed area. Therefore, we suspect that this phase dispersion in the interferometric time series probably expresses some temporal (likely seasonal) variations of ground motion that cannot be modeled by a constant deformation.

[38] More to the north, surface creep rapidly disappears between the latitude of profile P16 and the Wuhe Tableland. It gives rise to a smooth change in velocity gradient localized along the eastern flank of the Wuhe Tableland (P17 in Figure 7). This indicates that the active interseismic deformation between latitudes 23°25′ and 23°30′ progressively

migrates from the eastern side of the LV to its western side (i.e., the Wuhe Tableland). Moreover, there is no evidence of any other active fault west of these terraces.

3.3. North LV: From Rueisuei (Latitude 23°30′) to Hualien (Latitude 24°00′)

[39] The northern half of the LV deforms in a completely different way (Figure 9). From Rueisuei to Hualien, the PS velocity fields are almost uniform across the LV (profile P18 in Figure 10). In some places, a faint change in the velocity gradient may be detected along the western flank of the Coastal Range (profile P19 in Figure 10). Undoubtedly, this may be attributed to some elastic deformation along the northern segment of the LVF. However, this pattern can be detected only in a few places along the supposed fault trace. This may be simply due to the sparse distribution of PS on the hanging wall. Nevertheless, it is clear that the defor-
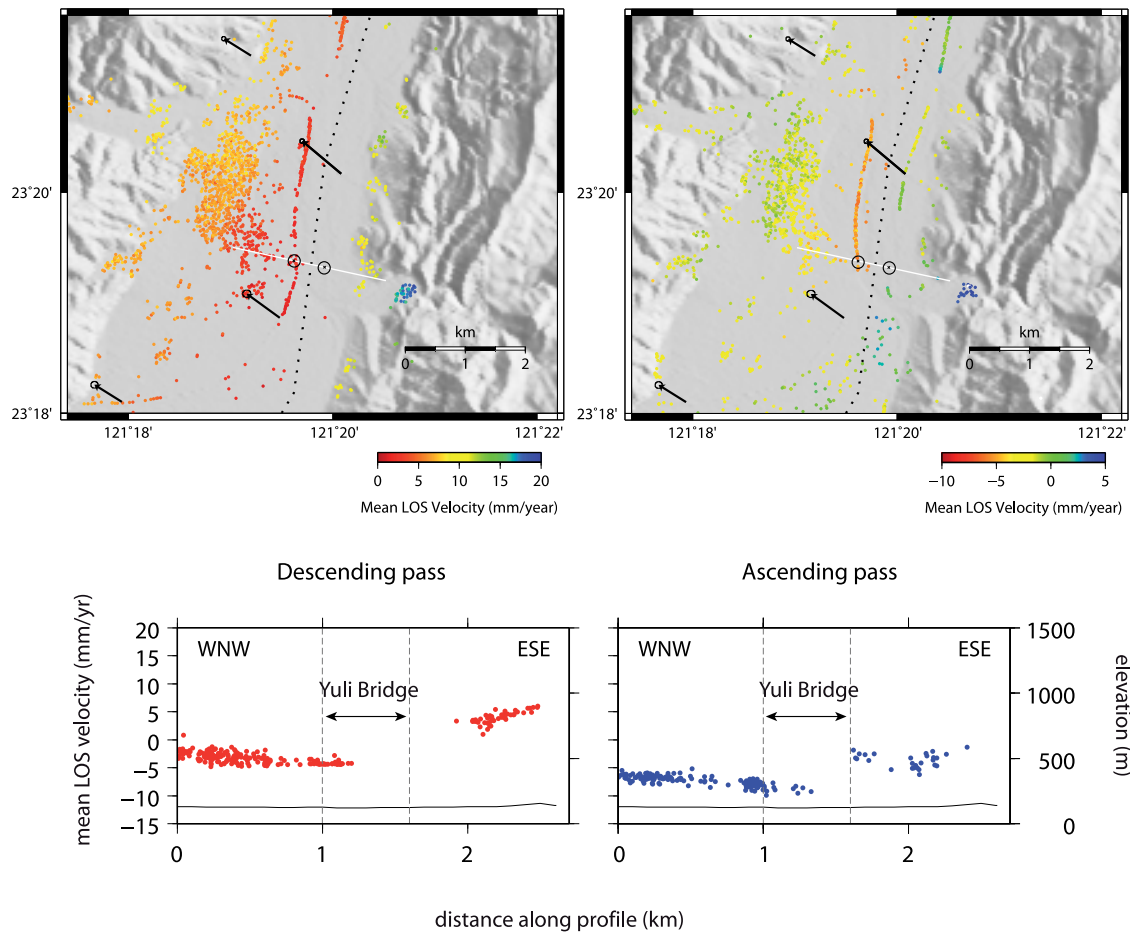
Figure 8. PS velocity map in (top left) the descending pass and (top right) the ascending pass around the Yuli Bridge. The white line shows the location of the profile that runs through the Yuli Bridge whose extremities are indicated with black circles. (bottom) The PS velocity profiles in both geometries. The vertical dotted lines indicate the location of the two extremities of the bridge. The LVF clearly runs below the bridge, within the riverbed.

mation across the LV is essentially distributed in a quasi–uniform way as expected in the case of a completely locked fault.

[40] The only other place where we found some local changes in the velocity gradients is in the Hualien area, close to the Milun terrace and just north of Hualien city (profiles P20 and P21 in Figure 10). These changes are small in amplitude but clearly above the noise level. The main feature in profile P20 is the large-scale change in velocity gradient observed in descending orbit. Deformation appears to be different on either side of the western flank of the Milun terrace and probably has a tectonic (interseismic) origin. A faint bend of the velocity profile in the ascending pass seems to confirm this interpretation. A few kilometers farther to the north, profile P21 shows a sharp discontinuity in the ascending pass. The sharp localization of this offset, as well as its temporal permanency, strongly suggests that it is related to the activity of the fault segments that border the Milun terrace. However, the origin of this very localized gradient should be confirmed by field works. The lack of PS on the western part of profile P21 in descending pass do not permit to confirm the large-scale velocity gradient change observed on profile P20.

4. Discussion

4.1. Three-Dimensional Velocity Maps

[41] The PS mean velocity fields estimated from the ascending and the descending orbits provide the relative ground motion along two independent directions. They can be combined to estimate the 3-D ground deformation. Because the PS locations are not the same in both LOS, we interpolate locally each PS velocity data set on a fine (1 s) regular grid.

[42] Furthermore, to retrieve the 3-D components of the surface deformation, an additional constraint is required. We impose the horizontal azimuth for the PS velocities by simply interpolating [*Smith and Wessel*, 1990] the azimuth of the GPS velocity field [*Huang et al.*, 2010]. We select a tension factor (which characterizes the rigidity of the inter-polated surface) equal to 0.2. This guarantees a good fit at GPS sites and a smooth spatial interpolation at large scale altogether. This interpolation is not reliable far from GPS
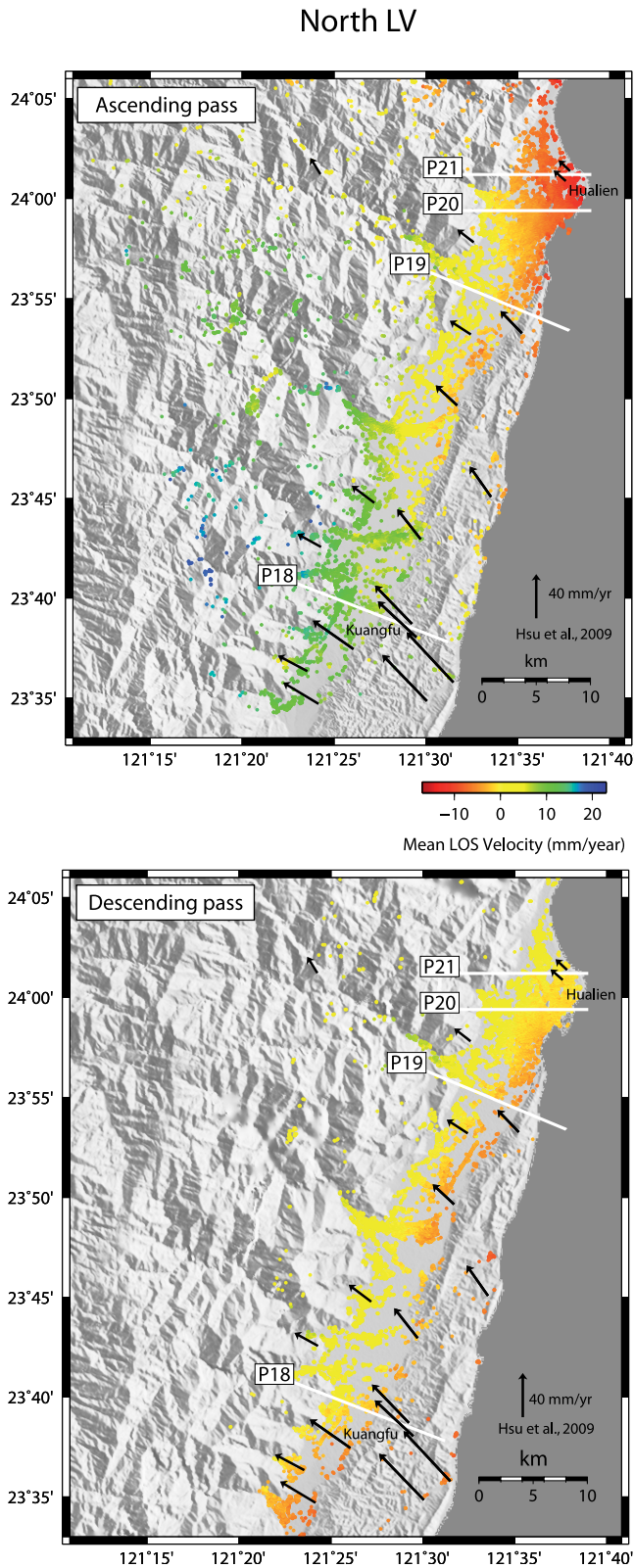
Figure 9. PS velocity map in (top) the ascending pass and (bottom) the descending pass between Rueisuei and Hualien. GPS velocity field is from *Hsu et al.* [2009b]. White lines show the location of the profiles presented in the Figure 10.

sites and in the vicinity of rapid azimuth changes. However, because the large-scale azimuth field is rather regular and the density of GPS sites close to the LVF is high enough to limit local artifacts, we think that our results are reliable.

[43] Finally, we project the 3-D GPS velocity vectors [*Huang et al.*, 2010] along each LOS and compare them with the corresponding PS velocity measurements. This allows to estimate, in a least squares sense, the best planar correction to apply to the PS velocity fields to, first, adjust them to the same reference frame as GPS velocities, and second, remove any possible orbital residue.

[44] For each element of the PS grid, the 3-D components of the velocity vector can now be easily obtained by solving the following linear system:

$$\begin{cases} \phi^{(\mathrm{asc})} = \mathrm{LOS}^{(\mathrm{asc})} \cdot (Vx, Vy, Vz) \\ \phi^{(\mathrm{desc})} = \mathrm{LOS}^{(\mathrm{desc})} \cdot (Vx, Vy, Vz) \\ Vy = \tan(\alpha)Vx \end{cases}$$

where (Vx, Vy, Vz) is the 3-D velocity vector, $\mathrm{LOS}^{(\mathrm{asc})}$ and $\mathrm{LOS}^{(\mathrm{desc})}$ are the local look angle vectors in the ascending and the descending pass, the dot symbol indicates the scalar product, $\phi^{(\mathrm{asc})}$ and $\phi^{(\mathrm{desc})}$ are the PS mean velocities in both geometries corrected for a plane as described before, and α is the azimuth of the horizontal velocity as estimated from GPS.

[45] E-W velocities estimated at GPS sites both from GPS measurements and PS velocities combination (Figure 11) are in good agreement. The RMS is 3 and 5 mm/yr in the northern and southern parts of the LV, respectively. The only major misfit concerns the GPS site (S073 in Huang's GPS network) located within the LV at latitude 23°14′. We have no argument to determine which of the two measurements is correct.

[46] The 3-D velocity fields derived from our PS analysis are presented in Figures 12 and 13. The PS and GPS [*Huang et al.*, 2010] horizontal velocity fields are expressed relative to the Paisha Island in Penghu, on the Chinese continental margin.

[47] The southern end of the Coastal Range (from the latitude of Luyeh 22°54′ to the Taitung plain) is characterized by rapid uplift (~10 mm/yr) relative to the LV and the Taitung plain. This pattern of vertical deformation is clearly bounded to the west by the Luyeh Strand fault zone. In agreement with the interpretation of the PS velocity profiles developed in section 3.1, most of the uplift rate (~7 mm/yr) occurs along the Luyeh Strand fault zone, while the remainder (~3 mm/yr) is accommodated by the Peinan Strand fault zone. By contrast, the north component of deformation is essentially accommodated by the Peinan Strand. Hence even though both strands accommodate sinistral and reverse motions, our 3-D map indicates that in this area there is some partitioning between the strain across the Luyeh Strand, which is dominated by nearly pure thrusting, and the strain across the Peinan Strand which is dominated by strike-slip shearing. This conclusion is in agreement with other geologic and geodetic studies [e.g., *Lee et al.*, 1998; *Hu et al.*, 2001; *Shyu et al.*, 2008].

[48] Farther to the north, the region located between Chihshang and Rueisuei exhibits a subsidence rate relative
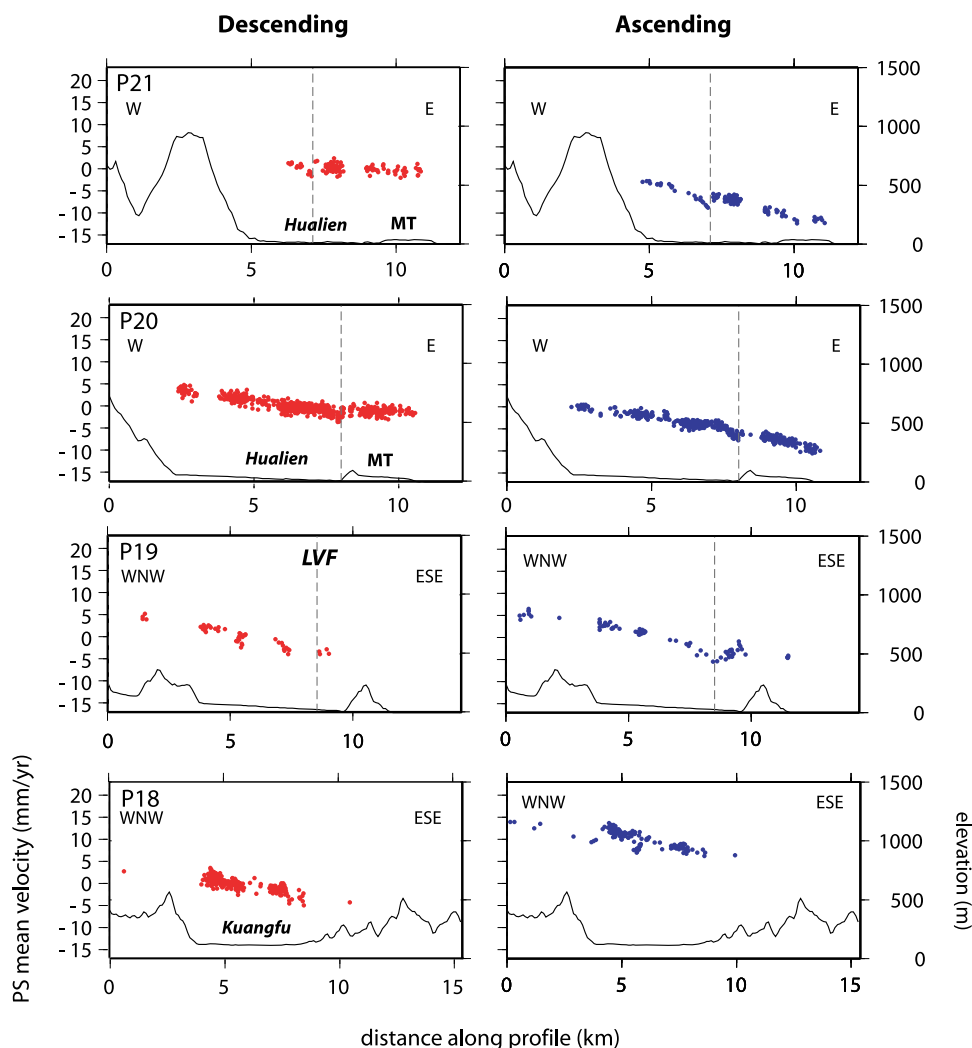
Figure 10. Profiles of PS mean velocities between Rueisuei and the Hualien plain in (left) the descending pass and (right) the ascending pass, superimposed on the topographic profile from the TWD67 40 m resolution digital elevation model. The locations of these profiles are shown in Figure 9. Black dotted lines indicate the location of significant velocity gradient changes in the PS velocity maps. MT, Milun Terraces.

to the Coastal Range with similar amplitude (~10 mm/yr). This estimate is in good agreement with leveling measurements [e.g., *Liu and Yu*, 1990; *Yu and Kuo*, 2001; *Chen et al.*, 2004] that indicate an uplift of the Coastal Range relative to the LV due to the activity of the east dipping reverse LVF.

[49] This central zone of the LV is also subsiding at the same rate with respect to the Taitung plain. This northward gradient of deformation within the LV also exists within the Coastal Range. However, this low-amplitude and large-scale gradient is essentially controlled by the set of GPS velocities used for correcting the PS velocities from any likely orbital residues. Hence, in this case, we simply establish that the PS vertical velocities are compatible with the vertical motion measured by GPS [*Huang et al.*, 2010] and confirmed by the leveling data along the east coast [see *Wu et al.*, 2009, Figure 10].

[50] Overall, the agreement between GPS and PS vertical velocities is good (rms ~5 mm/yr). This is notably the case all along the coast and south of 23°00′. The only significant difference arises along the LVF north of 23°00′ where GPS indicate a slightly higher relative vertical motion across the LVF (~15 mm/yr) than the analogous PS do (~10 mm/yr). This is notably the case in the Yuli area (latitude ~23°18′) where some GPS sites measured a high uplift rate of about 5 to 10 mm/yr on the hanging wall of the LVF which is not captured by our PS analysis. Because there is high uncertainty in the vertical GPS measurements (about 5 to 10 mm/yr illustrated by black circles in Figures 12 and 13), no definitive conclusion can be drawn about this discrepancy.

[51] To the north (Figure 13), the agreement between GPS and PS vertical motion is excellent (rms ~3 mm/yr). Both indicate a high subsidence rate of the Coastal Range (~15 mm/yr relative to the western side of the LV). As for
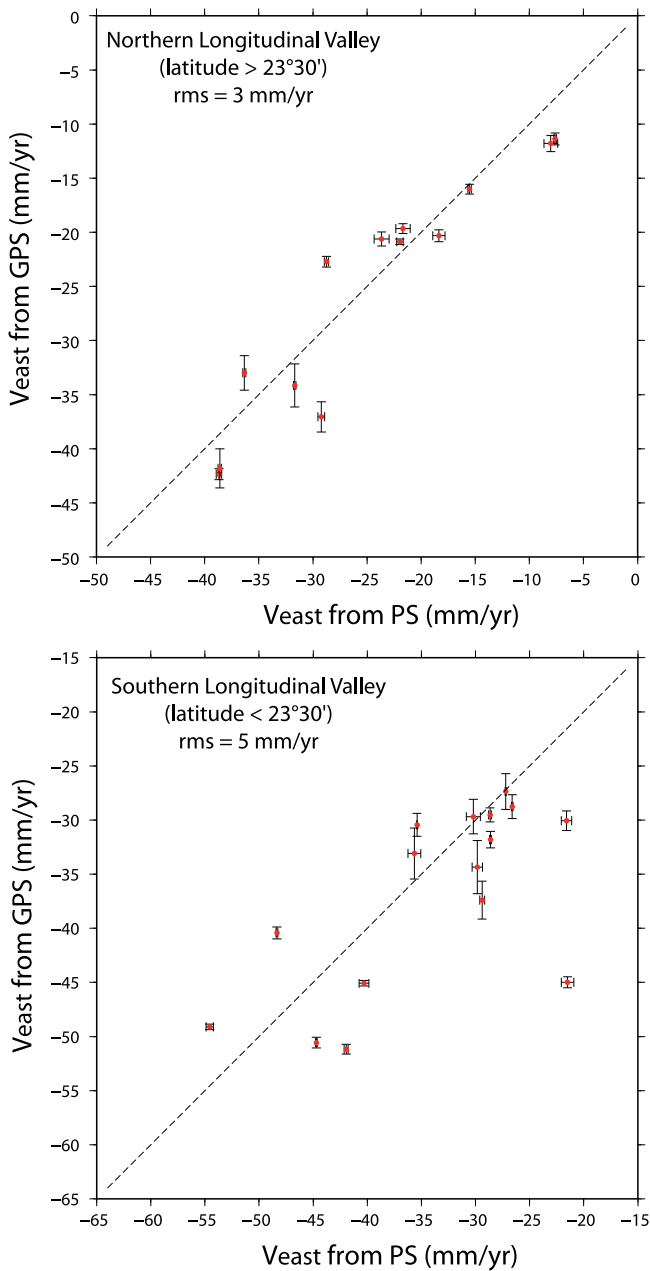
we detect a small wavelength pattern around latitude 23°42′ which indicates a faint relative uplift (~5 mm/yr) of the eastern side of the LV with respect to the general trend. This feature is stated by GPS and PS altogether.

[52] Regionally, the amplitude of the horizontal slip rate significantly decreases north of latitude 23°42′. These results agree with GPS velocity fields [e.g., *Bos et al.*, 2003; *Chang et al.*, 2003; *Hsu et al.*, 2009b; *Wu et al.*, 2009; *Huang et al.*, 2010]. This kinematic evolution is mostly related to the location of the intersection between the northward prolongation of the Luzon volcanic arc (LVA) and the eastern coast of Taiwan (close to latitude 23°45′) [*Wu et al.*, 2009]. South of this latitude, the LVA is located east of the LVF whereas, farther to the north, it is situated just beneath and even to the west of the LVF, north of Hualien. This feature induces significant deformation changes across this area due to the differential motion between the colliding and the subsiding domains.
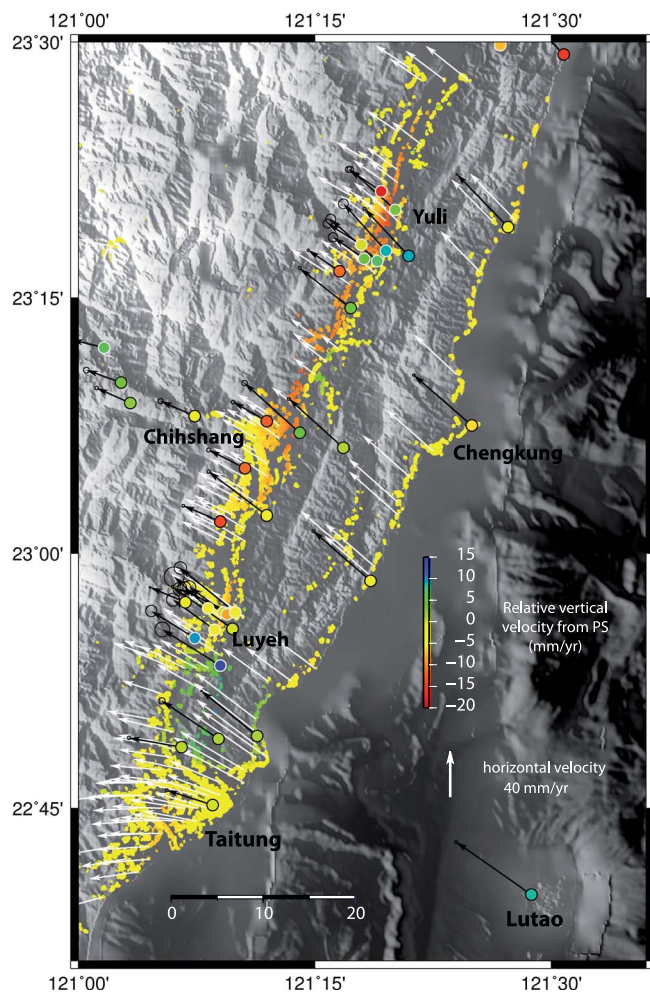
Figure 11. Comparison at GPS sites between the E-W velocities derived either from the combination of the ascending and the descending PS velocities or from the GPS time series analysis [*Huang et al.*, 2010]. Error bars for GPS measurements are the 1σ uncertainty. Error bars for PS velocities are the standard deviations estimated over the PS located within a certain radius. The minimum radius is set to 100 m. We increase it until at least 10 PS are found. The maximum radius is set to 2 km. If there are still less than 10 PS for such a maximum radius, the GPS site is not selected for this plot. The RMS is 3 and 5 mm/yr in the northern and southern part of the LV, respectively.

the south-north gradient discussed in the southern part of the LV, this long wavelength feature is probably mainly controlled by GPS when correcting the PS velocity fields using a constant gradient pattern over the whole scene. However,

Figure 12. The 3-D velocity map in the southern part of the LV. White arrows represent the horizontal motion estimated from PS. Black arrows are GPS velocity vectors from *Huang et al.* [2010]. The vertical motion estimated from PS (open circles) and GPS (black circles for uncertainty higher than 5 mm/yr; otherwise, white circles) is displayed using the rainbow color palette.

Figure 13. The 3-D velocity map in the northern part of the LV. White arrows represent the horizontal motion estimated from PS. Black arrows are GPS velocity vectors from *Huang et al.* [2010]. The vertical motion estimated from PS (open circles) and GPS (black circles for uncertainty higher than 5 mm/yr; otherwise, white circles) is displayed using the rainbow color palette.
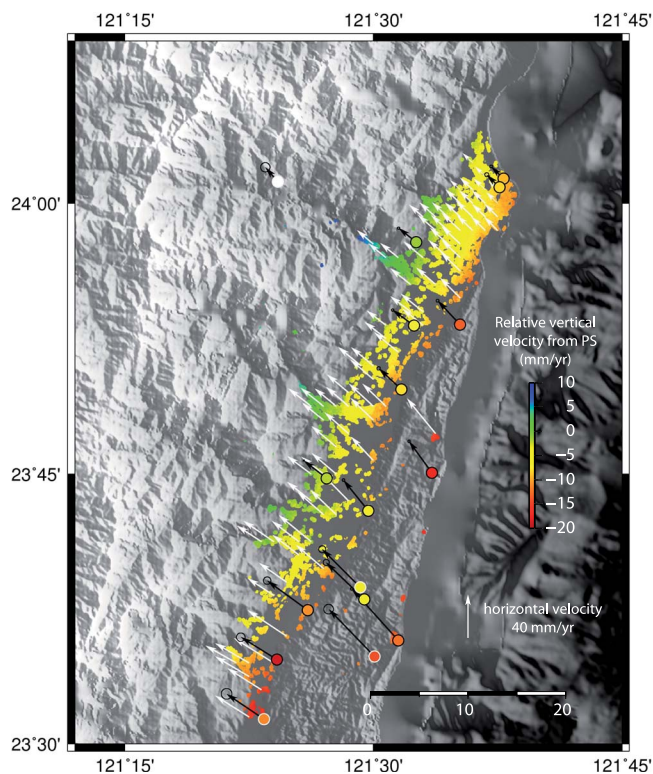
4.2. Surface Slip Along the Creeping Segment in the Middle of the LVF

[53] Many models of slip distribution at depth have been proposed either at the scale of the whole island or at regional scale [e.g., *Yu et al.*, 1990; *Lee and Angelier*, 1993; *Hu et al.*, 1996 and 1997; *Chemenda et al.*, 2001; *Ding et al.*, 2001; *Hsu et al.*, 2003; *Johnson et al.*, 2005]. Such a detailed slip modeling is out of the scope of this paper. Here, we rather focus on the creeping segment in the middle of the LVF to estimate the surface slip along the fault plane using the PS velocity offsets measured in the vicinity of the LVF in the ascending and the descending pass.

[54] We impose the constraint that the slip vector that induced the observed velocity offset must lay along the fault plane. The strike of this plane is determined by the trace of the fault at the surface (25°W in average), while its dip angle at the surface is imposed to 55° to the east as suggested by various authors [e.g., *Tsai*, 1986; *Liu and Yu*, 1990; *Lee and Angelier*, 1993; *Rau and Wu*, 1995; *Angelier et al.*, 1997; *Chen and Rau*, 2002; *Kuochen et al.*, 2004; *Wu et al.*, 2007].

[55] The along-strike evolution of the velocity offset in the descending pass (Figure 14a) is comparable to previous results [*Hsu and Bürgmann*, 2006]. We significantly improve it by including the profile obtained in the ascending pass which shows a very different shape. Indeed, the

velocity offset becomes significantly lower compared to the descending pass north of Chihshang. This can be explained by an increasing fault-parallel motion partly collinear to the ascending LOS but almost perpendicular to the descending LOS. In this way, the hanging wall of the LVF moves toward the satellite vertically but away from it horizontally resulting in a reduced offset in ascending geometry relatively to the descending one. This interpretation is confirmed by the slight change in azimuth of the GPS velocity vectors located east of the LVF at the latitude of Yuli, with respect to the other vectors across the Coastal Range (Figure 12).

[56] This effect is highlighted by our estimate of the surface slip along the fault plane (Figure 14b). North of latitude 23°12′, the rake is about 70° (Figure 14c) with mean slip amplitude of ~25 mm/yr. These results are in accordance with those obtained from leveling data [*Liu and Yu*, 1990], detailed surveys of faulted concrete structures [*Lee and Angelier*, 1993], or GPS velocity fields [e.g., *Bos et al.*, 2003; *Chang et al.*, 2003; *Hsu et al.*, 2009b]. The slip amplitude increases gradually from latitude 23°00′ to 23°16′, before decreasing down to zero at latitude 23°27′.

[57] The shallow microseismicity (i.e., magnitude less than 3 and depth lower than 10 km) in the vicinity of the LV [*W. H. Q. Lee et al.*, 2001] between 1992 and 1999 (prior to Chi-Chi earthquake) can be used to investigate the spatial segmentation of the LVF aseismic creeping segment (Figure 14d). This microseismicity is in good agreement with the observed velocity offsets. Indeed, south of 23°04′ and north of 23°24′ the low surface creep rate (~10 mm/yr) is related to intense shallow seismic activity. On the contrary, between 23°09′ and 23°24′, the fault segment of the LVF that creeps the most (~25 mm/yr) is related to aseismic creep at the shallow 10 km crust. Finally, in between these two segments (23°04′ to 23°09′), seismicity reveals a distinct peak of activity. This area probably corresponds to a relay zone between two segments with different mechanical behaviors and creep rates.

[58] South of latitude 22°57′, the LVF and its two southern strands seem to be locked even though it is at shallow depth. Inversion of these new PS velocity fields is now required to assess the associated slip distribution at depth all along the LVF.

4.3. Comparison With ALOS Data

[59] In this paper, we limited our processing to the ERS archives. However, this study can be extended to other or longer radar time series. Preliminary comparison of our results with first results using the ascending *L* band SAR data acquired by ALOS satellite over the period 2007–2010 and analyzed with StaMPS method [*Champenois et al.*, 2010] shows similar patterns. The amplitude of the velocity offset across the LVF is globally compatible in both studies. However, some differences like the presence of surface creep close to the Wuhe Tableland in the ALOS data, contrary to our study, suggest some changes of interseismic behavior between the periods 1993–1999 and 2007–2010. The occurrence of the 10 December 2003 Chengkung (Mw 6.8) and 1 April 2006 Taitung earthquakes (Mw 6.1) may explain this change. More detailed investigation including the PS analysis of the complete radar time series including the ERS, Envisat, and ALOS acquisitions should
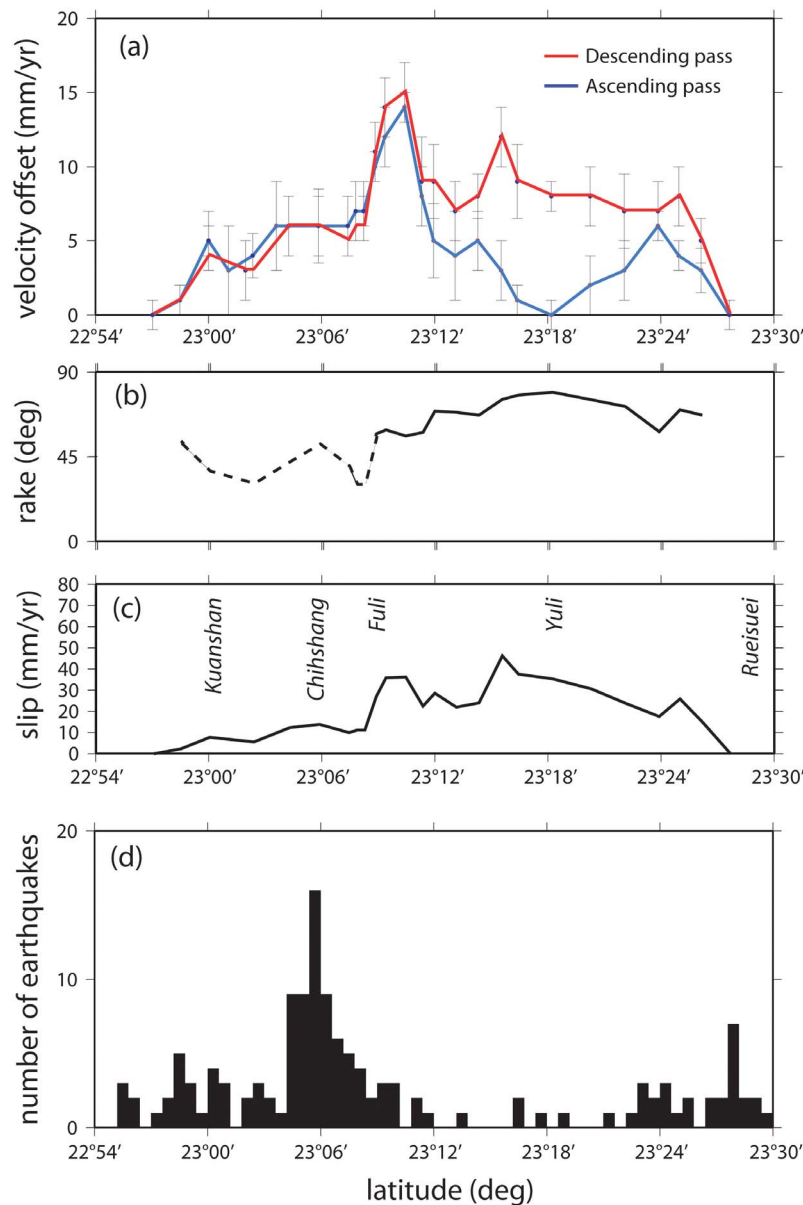
Figure 14. (a) Evolution of surface creep motion in ascending and descending pass, along the fault trace. (b) Associated rake and (c) slip amplitude estimated when imposing a fault dip angle of 55° to the east. (d) Histogram of shallow earthquakes (M < 3 and depth lower than 10 km) along the creeping segment of the LVF during the time interval spanned by our study [from *W. H. Q. Lee et al.*, 2001].

provide significant insights into the fine-scale temporal evolution of the LVF behavior.

5. Conclusions

[60] This study presents the interseismic velocity fields along the eastern central coast of Taiwan derived from a PS-InSAR analysis of the ERS archives (1993–1999). Contrary to the standard InSAR approach that faces the very restrictive limitations of vegetation coverage and atmospheric changes, the PS-InSAR technique succeeded in mapping the active faults and deformation all along the Longitudinal Valley (LV) and Coastal Range of Taiwan with a resolution of a few tens of meters. Even when selecting PS with stringent criteria, the spatial density of the PS remains very high (more than 10 PS per square kilometer). The relative velocity changes along the satellite LOS have been measured with a precision better than ~2 mm/yr as stated by the spatial distribution of the temporal standard deviation of the radar phase with respect to the mean velocity estimated by StaMPS. The only noticeable exception concerns the central part of the creeping segment around Yuli between latitudes 23°09′ and 23°15′, in ascending orbits. This may be due to temporal (likely seasonal) variations of ground motion that cannot be modeled by a constant deformation. Capturing such a transient phenomenon would be very useful to better understand the fault mechanical behavior along this creeping segment.
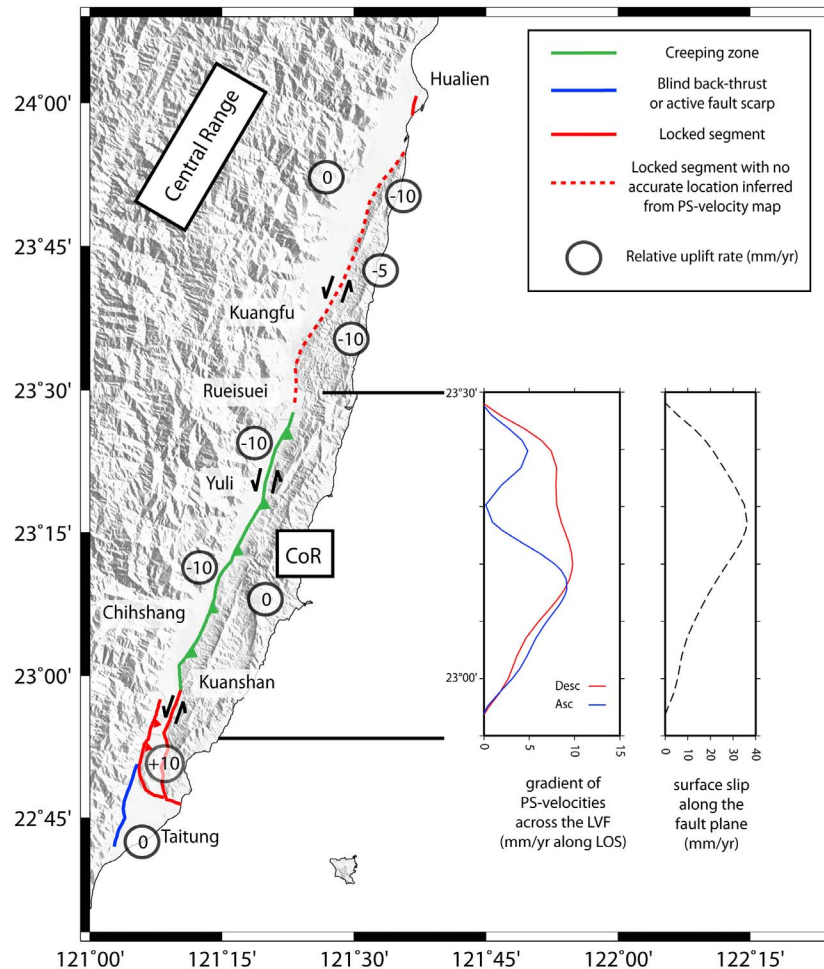
Figure 15. Schematic view of the surface deformation and the fault activity along the LV from our PS analysis. The significance of colored segments and black circles is provided in the upper right legend. The two profiles along the central creeping segment of the LV are a smoothed version of those presented in Figure 14.

[61] The precise location of PS velocity gradient changes has permitted to accurately map the active fault segments all along the LV (Figure 15). About 5 mm/yr of deformation is accommodated west of the Taitung plain (TP) along a segment which is probably a blind southward prolongation of the Central Range Fault (CRF). North of the TP, the southern termination of the LVF runs eastward along the southern tip of the Coastal Range and probably connects offshore with the reverse faults and backthrusts trending N-S that affect the Huatung ridge and the Taitung trough. No other active segment has been detected across the TP. Between the TP and Kuanshan, deformation is localized along the Luyeh Strand (west of the LV) and the Peinan Strand (east of the LV). The narrow PS velocity gradients across these fault segments indicate that their locking depths are probably very shallow. Farther north, between Kuanshan and Rueisuei, the deformation is essentially accommodated by the LVF that runs along the western flank of the Coastal Range. The sharp discontinuities of the PS velocity fields across the LVF indicate that these segments are creeping, with some likely seasonal effects in the nearby of Fuli village. South of Rueisuei, the main deformation progressively

moves toward the western side of the LV along the eastern flank of the Wuhe Tableland. Then, from Rueisuei to Hualien, despite the scarcity of PS within the Coastal Range, PS velocity fields indicate that the ground deformation across the LV is essentially diffuse as expected for a completely locked fault. Finally, evidence of localized deformation within the Hualien plain has been found, notably along the western flank of the Milun terrace. All these results are in good agreement with the available geodetic and geomorphological studies of the LV. Consequently, they constitute a valuable complementary data set for understanding the tectonic deformation in this area.

[62] While we have been able to describe in detail the activity of the Longitudinal Valley Fault (LVF), at the opposite, we did not find clear evidence for present-day activity of the CRF. The only exceptions may be found along the Peinanshan Terraces and south of Rueisuei along the eastern flank of the Wuhe Tableland. Southwest of Taitung, PS reveals a clear deformation pattern along the eastern flank of the Central Range (CR), but, because the deformation gradient is relatively low, we attribute it to diffuse blind back thrusting. Elsewhere along the LV, no

significant deformation has been detected along the eastern flank of the CR. Even though this may be attributed to the lack of PS within the CR, we rather believe that crustal shortening across the LV is presently mainly accommodated along the LVF on the eastern side of the valley.

[63] We estimated a 3-D velocity map all along the LV by combining the PS velocity fields obtained in ascending and descending pass and introducing horizontal azimuth constraints from GPS. The main results are summarized in Figure 15. This data set suggests a large uplift of the southern Coastal Range relative to the LV, while it confirms the increasing subsidence of the central part of both the LV and the Coastal Range from south to north. Moreover, between Taitung and Luyeh, the Coastal Range and the LV itself experience significant uplift (~10 mm/yr). This vertical deformation is essentially accommodated along the Luyeh Strand while the strike-slip component of the deformation is rather accommodated along the Peinan Strand. Finally, north of Rueisuei, the Coastal Range uniformly subsides at ~15 mm/yr relative to the western side of the LV. However, a local uplift pattern (~5 mm/yr) appears around latitude 23°42′. This kinematic evolution is probably related to the location of the intersection between the northward prolongation of the Luzon volcanic arc and the eastern coast of Taiwan.

[64] Finally, we propose a rough estimate of the surface slip along the central creeping segment of the LVF. This estimate from PS measurements is in good agreement with similar inversions from geodetic or geological data. Moreover, shallow seismicity tends to confirm PS measurements which indicate that the creeping segments south and north of latitude 23°09′ behave slightly differently. We are currently working on a global inversion of the complete PS velocity fields that will undoubtedly provide very dense information about the interseismic slip distribution along the major fault segments of the LV. Together with other geodetic and geological data, these new accurate and spatially dense velocity fields help to better understand the spatial distribution of deformation all along the LV. They allow to precisely determine the kinematics of each fault segment, and consequently to improve seismic hazard assessment.

References

Adam, N., B. Kampes, and M. Eineder (2004), The development of a scientific Permanent Scatterer system: Modifications for mixed ERS/Envisat time series, in *Proceedings of the 2004 Envisat and ERS Symposium* [CD-ROM], edited by H. Lacoste and L. Ouwehand, *Eur. Space Agency Spec. Publ., ESA SP-572*, 73.1.

Angelier, J., H. T. Chu, and J. C. Lee (1997), Shear concentration in a collision zone: Kinematics of the Chihshang Fault as revealed by outcrop-scale quantification of active faulting, Longitudinal Valley, eastern Taiwan, *Tectonophysics*, 274, 117–143, doi:10.1016/S0040-1951(96)00301-0.

Barrier, E., J. Angelier, H. T. Chu, and L. S. Teng (1982), Tectonic analysis of compressional structure in an active collision zone: The deformation of Pinanshan Conglomerates, eastern Taiwan, *Proc. Geol. Soc. China*, 25, 123–138.

Bos, A. G., W. Spakman, and M. C. J. Nyst (2003), Surface deformation and tectonic setting of Taiwan inferred from a GPS velocity field, *J. Geophys. Res.*, 108(B10), 2458, doi:10.1029/2002JB002336.

Bürgmann, R., P. A. Rosen, and E. J. Fielding (2000), Synthetic Aperture Radar Interferometry to measure Earth's surface topography and its deformation, *Annu. Rev. Earth Planet. Sci.*, 28, 169–209, doi:10.1146/annurev.earth.28.1.169.

Champenois, J., B. Fruneau, E. Pathier, B. Deffontaines, K.-C. Lin, and J.-C. Hu (2010), Persistent Scatterer InSAR with ALOS data applied to the monitoring of the Longitudinal Valley Fault (Taiwan), paper presented at Geodynamics and Environment in East Asia International Conference and 6th Taiwan-France Earth Science Symposium, Univ. Paul Cézanne, Aix-en-Provence, France.

Chang, C. P., T. Y. Chang, J. Angelier, H. Kao, J. C. Lee, and S. B. Yu (2003), Strain and stress field in Taiwan oblique convergent system: Constraints from GPS observation and tectonic data, *Earth Planet. Sci. Lett.*, 214, 115–127, doi:10.1016/S0012-821X(03)00360-1.

Chemenda, A. I., R. K. Yang, J. F. Stephan, E. A. Konstantinovskaya, and G. M. Ivanov (2001), New results from physical modelling of arc-continent collision in Taiwan: Evolutionary model, *Tectonophysics*, 333(1–2), 159–178, doi:10.1016/S0040-1951(00)00273-0.

Chen, H., and R. Rau (2002), Earthquake locations and style of faulting in an active arc-continent plate boundary: The Chihshang fault of eastern Taiwan, *Eos Trans. AGU*, 83(47), Fall. Meet. Suppl., Abstract T61B–1277.

Chen, H. Y., S. B. Yu, Y. G. Chen, Y. R. Chuang, and H. Y. Hu (2004), GPS measurements of near-fault crustal deformation in the south Longitudinal Valley, southeastern Taiwan, paper presented at 2004 International Symposium on GNSS/GPS, Univ. of New South Wales, Sydney, Australia.

Chen, H. Y., S. B. Yu, L. C. Kuo, and C. C. Liu (2006), Coseismic and postseismic surface displacements of the 10 December 2003(Mw 6.5) Chengkung, eastern Taiwan, earthquake, *Earth Planets Space*, 58, 5–21.

Cheng, L.-W., J.-C. Lee, J.-C. Hu, and H.-Y. Chen (2009), Coseismic and postseismic slip distribution of the 2003 Mw = 6.5 Chengkung earthquake in eastern Taiwan: Elastic modelling from inversion of GPS data, *Tectonophysics*, 466, 335–343, doi:10.1016/j.tecto.2007.11.021.

Cheng, S. N., Y. T. Yeh, and M. S. Yu (1996), The 1951 Taitung earthquake in Taiwan, *J. Geol. Soc. China*, 39(3), 267–285.

Chung, L.-H., Y.-G. Chen, Y.-M. Wu, J. B. H. Shyu, Y.-T. Kuo, and Y.-N. N. Lin (2008), Seismogenic faults along the major suture of the plate boundary deduced by dislocation modelling of coseismic displacements of the 1951 M7.3 Hualien-Taitung earthquake sequence in eastern Taiwan, *Earth Planet. Sci. Lett.*, 269, 416–426, doi:10.1016/j.epsl.2008.02.035.

Colesanti, C., A. Ferretti, F. Novali, C. Prati, and F. Rocca (2003), SAR monitoring of progressive and seasonal ground deformation using the permanent scatterer technique, *IEEE Trans. Geosci. Remote Sens.*, 41(7), 1685–1701, doi:10.1109/TGRS.2003.813278.

Crespi, J. M., Y. C. Chan, and M. S. Swaim (1996), Synorogenic extension and exhumation of the Taiwan hinterland, *Geology*, 24, 247–250, doi:10.1130/0091-7613(1996)024<0247:SEAEOT>2.3.CO;2.

Ding, Z. Y., Y. Q. Yang, Z. X. Yao, and G. H. Zhang (2001), A thin-skinned collisional model for the Taiwan orogeny, *Tectonophysics*, 332, 321–331, doi:10.1016/S0040-1951(00)00289-4.

Ferretti, A., C. Prati, and F. Rocca (1999), Permanent scatterers in SAR interferometry, paper presented at International Geoscience and Remote Sensing Symposium, IEEE, Hamburg, Germany.

Ferretti, A., C. Prati, and F. Rocca (2000), Nonlinear subsidence rate estimation using permanent scatterers in differential SAR interferometry, *IEEE Trans. Geosci. Remote Sens.*, 38(5), 2202–2212, doi:10.1109/36.868878.

Ferretti, A., C. Prati, and F. Rocca (2001), Permanent scatterers in SAR interferometry, *IEEE Trans. Geosci. Remote Sens.*, 39(1), 8–20, doi:10.1109/36.898661.

Ho, C. S. (1986), A synthesis of the geologic evolution of Taiwan, *Tectonophysics*, 125, 1–16, doi:10.1016/0040-1951(86)90004-1.

Ho, C. S. (1988), *An Introduction to the Geology of Taiwan, Explanatory Text of the Geologic Map of Taiwan*, 2nd ed., 192 pp., Cent. Geol. Surv., Taipei, Taiwan.

Hooper, A. J. (2006), Persistent scatterer radar interferometry for crustal deformation studies and modelling of volcanic deformation, Ph.D. thesis, Stanford Univ., Stanford, Calif.

Hooper, A., H. Zebker, P. Segall, and B. Kampes (2004), A new method for measuring ground deformation on volcanoes and other natural terrains using InSAR persistent scatterers, *Geophys. Res. Lett.*, 31, L23611, doi:10.1029/2004GL021737.

Hooper, A., P. Segall, and H. Zebker (2007), Persistent scatterers InSAR for crustal deformation analysis, with application to Volcan Alcedo, Galapagos, *J. Geophys. Res.*, *112*, B07407, doi:10.1029/2006JB004763.

Hsu, L., and R. Bürgmann (2006), Surface creep along the Longitudinal Valley fault, Taiwan from InSAR measurements, *Geophys. Res. Lett.*, *33*, L06312, doi:10.1029/2005GL024624.

Hsu, Y.-J., M. Simons, S.-B. Yu, L.-C. Kuo, and H.-Y. Chen (2003), A two-dimensional dislocation model for interseismic deformation of the Taiwan mountain belt, *Earth Planet Sci. Let.*, *211*, 287–294, doi:10.1016/S0012-821X(03)00203-6.

Hsu, Y.-J., S.-B. Yu, and H.-Y. Chen (2009a), Coseismic and postseismic deformation associated with the 2003 Chengkung, Taiwan earthquake, *Geophys. J. Int.*, *176*, 420–430, doi:10.1111/j.1365-246X.2008.04009.x.

Hsu, Y.-J., S.-B. Yu, M. Simons, L.-C. Kuo, and H.-Y. Chen (2009b), Interseismic crustal deformation in the Taiwan plate boundary zone revealed by GPS observations, seismicity, and earthquake focal mechanisms, *Tectonophysics*, *479*, 4–18, doi:10.1016/j.tecto.2008.11.016.

Hu, J. C., J. Angelier, J. C. Lee, H. T. Chu, and D. Byrne (1996), Kinematics of convergence, deformation and stress distribution in the Taiwan collision area: 2-D finite-element numerical modeling, *Tectonophysics*, *255*, 243–268, doi:10.1016/0040-1951(95)00140-9.

Hu, J. C., J. Angelier, and S. B. Yu (1997), An interpretation of the active deformation of southern Taiwan based on numerical simulation and GPS studies, *Tectonophysics*, *274*, 145–169, doi:10.1016/S0040-1951(96)00302-2.

Hu, J. C., S. B. Yu, J. Angelier, and H. T. Chu (2001), Active deformation of Taiwan from GPS measurements and numerical simulations, *J. Geophys. Res.*, *106*, 2265–2280, doi:10.1029/2000JB900196.

Huang, C.-Y., W.-Y. Wu, C.-P. Chang, S. Tsao, P. B. Yuan, C.-W. Lin, and X. Kuan-Yuan (1997), Tectonic evolution of accretionary prism in the arc-continent collision terrane of Taiwan, *Tectonophysics*, *281*, 31–51, doi:10.1016/S0040-1951(97)00157-1.

Huang, W.-J., K. M. Johnson, J. Fukuda, and S.-B. Yu (2010), Insights into active tectonics of eastern Taiwan from analyses of geodetic and geologic data, *J. Geophys. Res.*, *115*, B03413, doi:10.1029/2008JB006208.

Johnson, K. M., P. Segall, and S. B. Yu (2005), A viscoelastic earthquake cycle model for Taiwan, *J. Geophys. Res.*, *110*, B10404, doi:10.1029/2004JB003516.

Kampes, B. M. (2005), Displacement parameter estimation using permanent scatterer interferometry, Ph.D. thesis, Delft Univ. of Technol., Delft, Netherlands.

Kampes, B. M., R. F. Hanssen, and Z. Perski (2003), Radar interferometry with public domain tools, paper presented at Third International Workshop on ERS SAR Interferometry, Eur. Space Agency, Frascati, Italy.

Kao, H., and P. R. Jian (2001), Seismogenic patterns in the Taiwan region: Insights from source parameter inversion of BATS data, *Tectonophysics*, *333*, 179–198, doi:10.1016/S0040-1951(00)00274-2.

Kao, H., S. S. J. Shen, and K. F. Ma (1998), Transition from oblique subduction to collision: Earthquakes in the southernmost Ryukyu arc-Taiwan region, *J. Geophys. Res.*, *103*, 7211–7229, doi:10.1029/97JB03510.

Kuochen, H., Y. M. Wu, C. H. Chang, J. C. Hu, and W. S. Chen (2004), Relocation of the eastern Taiwan earthquakes and its tectonic implications, *Terr. Atmos. Oceanic Sci.*, *15*, 647–666.

Lallemand, S., Y. Font, H. Bijwaard, and H. Kao (2001), New insights on 3-D plates interaction near Taiwan from tomography and tectonic implications, *Tectonophysics*, *335*, 229–253, doi:10.1016/S0040-1951(01)00071-3.

Lee, J. C., and J. Angelier (1993), Location of active deformations and geodetic data analyses: An example of the Longitudinal Valley Fault, Taiwan, *Bull. Soc. Geol. Fr.*, *164*(4), 533–540.

Lee, J. C., J. Angelier, H. T. Chu, S. B. Yu, and J. C. Hu (1998), Plate boundary strain partitioning along the sinistral suture of the Philippine and Eurasian plates: Analysis of geodetic data and geological observations, *Tectonics*, *17*, 859–871, doi:10.1029/98TC02205.

Lee, J. C., J. Angelier, H. T. Chu, J. C. Hu, and F. S. Jeng (2001), Continuous monitoring of an active fault in a plate suture zone: A creepmeter study of the Chihshang Fault, eastern Taiwan, *Tectonophysics*, *333*, 219–240, doi:10.1016/S0040-1951(00)00276-6.

Lee, J. C., J. Angelier, H. T. Chu, J. C. Hu, F. S. Jeng, and R. J. Rau (2003), Active fault creep variations at Chihshang, Taiwan, revealed by creep meters monitoring, 1998–2001, *J. Geophys. Res.*, *108*(B11), 2528, doi:10.1029/2003JB002394.

Lee, W. H. Q., T. C. Shin, K. W. Kuo, K. C. Chen, and C. F. Wu (2001), Data files from CWB free-field strong-motion data from the 21 September Chi-Chi, Taiwan, earthquake, *Bull. Seismol. Soc. Am.*, *91*(5), 1390, doi:10.1785/0120000756.

Liu, C. C., and S. B. Yu (1990), Vertical crustal movements in eastern Taiwan and their tectonic implications, *Tectonophysics*, *183*, 111–119, doi:10.1016/0040-1951(90)90191-A.

Lyons, S., and D. Sandwell (2003), Fault creep along the southern San Andreas from interferometric synthetic aperture radar, permanent scatterers, and stacking, *J. Geophys. Res.*, *108*(B1), 2047, doi:10.1029/2002JB001831.

Malavieille, J., and G. Trullenque (2009), Consequences of continental subduction on forearc basin and accretionary wedge deformation in SE Taiwan: Insights from analogue modeling, *Tectonophysics*, *466*(3–4), 377–394, doi:10.1016/j.tecto.2007.11.016.

Malavieille, J., S. E. Lallemand, S. Dominguez, A. Deschamps, C.Y. Lu, C. S. Liu, P. Schnürle, and the ACT scientific crew (2002), Arc-continent collision in Taiwan: New marine observations and tectonic evolution, in *Geology and Geophysics of an Arc-Continent Collision, Taiwan*, edited by T. B. Byrne and C. S. Liu, *Geol. Soc. Am. Spec. Pap.*, *358*, 187–211.

Massonnet, D., and K. Feigl (1998), Radar interferometry and its application to changes in the earth's surface, *Rev. Geophys.*, *36*(4), 441–500, doi:10.1029/97RG03139.

Mozziconacci, L., B. Delouis, J. Angelier, J. C. Hu, and B. S. Huang (2009), Slip distribution on a thrust fault at a plate boundary: The 2003 Chengkung earthquake, Taiwan, *Geophys. J. Int.*, *177*, 609–623, doi:10.1111/j.1365-246X.2009.04097.x.

Rau, R. J., and F. T. Wu (1995), Tomographic imaging of lithospheric structures under Taiwan, *Earth Planet. Sci. Lett.*, *133*, 517–532, doi:10.1016/0012-821X(95)00076-O.

Rosen, P. A., S. Henley, G. Peltzer, and M. Simons (2004), Updated repeat orbit interferometry package released, *Eos Trans. AGU*, *85*(5), 47, doi:10.1029/2004EO050004.

Shyu, J. B. H., K. Sieh, Y.-G. Chen, and C.-S. Liu (2005), Neotectonic architecture of Taiwan and its implications for future large earthquakes, *J. Geophys. Res.*, *110*, B08402, doi:10.1029/2004JB003251.

Shyu, J. B. H., K. Sieh, J. P. Avouac, W. S. Chen, and Y. G. Chen (2006a), Millenial slip rate of the Longitudinal Valley fault from river terraces: Implications for convergence across the active suture of eastern Taiwan, *J. Geophys. Res.*, *111*, B08403, doi:10.1029/2005JB003971.

Shyu, J. B. H., K. Sieh, Y. G. Chen, and L. H. Cheung (2006b), Geomorphic analysis of the Central Range fault, the second major active suture of the Longitudinal Valley suture, eastern Taiwan, *Geol. Soc. Am. Bull.*, *118*, 1447–1462, doi:10.1130/B25905.1.

Shyu, J. B. H., L.-H. Chung, Y.-G. Chen, J.-C. Lee, and K. Sieh (2007), Re-evaluation of the surface ruptures of the November 1951 earthquake series in eastern Taiwan, and its neotectonic implications, *J. Asian Earth Sci.*, *31*, 317–331, doi:10.1016/j.jseaes.2006.07.018.

Shyu, J. B. H., K. Sieh, Y. G. Chen, R. Y. Chuang, and L. H. Chung (2008), Geomorphology of the southernmost Longitudinal Valley fault: Implications for evolution of the active suture of eastern Taiwan, *Tectonics*, *27*, TC1019, doi:10.1029/2006TC002060.

Smith, W. H. F., and P. Wessel (1990), Gridding with continuous curvature splines in tension, *Geophysics*, *55*, 293–305, doi:10.1190/1.1442837.

Suppe, J. (1981), Mechanics of mountain building and metamorphism in Taiwan, *Mem. Geol. Soc. China*, *4*, 67–89.

Teng, L. S. (1990), Geotectonic evolution of late Cenozoic arc-continent collision, *Tectonophysics*, *183*, 57–76, doi:10.1016/0040-1951(90)90188-E.

Tsai, Y. B. (1986), Seismotectonics of Taiwan, *Tectonophysics*, *125*, 1–16.

Van der Kooij, M., W. Hughes, S. Sato, and V. Poncos (2005), Coherent target monitoring at high spatial density, examples of validation results, paper presented at Fringe 2005, Eur. Space Agency, Frascati, Italy.

Werner, C., U. Wegmüller, T. Strozzi, and A. Wiesmann (2003), Interferometric point target analysis for deformation mapping, paper presented at Geoscience and Remote Sensing Symposium, IEEE, New York.

Wu, F. T., W.-T. Liang, J.-C. Lee, and H. Benz (2009), A model for the termination of the Ryukyu subduction zone against Taiwan: A junction of collision, subduction/separation, and subduction boundaries, *J. Geophys. Res.*, *114*, B07404, doi:10.1029/2008JB005950.

Wu, Y. M., Y. G. Chen, T. C. Shin, H. Kuochen, C. S. Hou, J. C. Hu, C. H. Chang, C. F. Wu, and T. L. Teng (2006), Coseismic versus interseismic ground deformations, fault rupture inversion and segmentation revealed by 2003 Mw 6.8 Chengkung earthquake in eastern Taiwan, *Geophys. Res. Lett.*, *33*, L02312, doi:10.1029/2005GL024711.

Wu, Y. M., C. H. Chang, L. Zhao, J. B. H. Shyu, Y. C. Chen, K. Sieh, and J. P. Avouac (2007), Seismic tomography of Taiwan: Improved constraints from a dense network of strong motion stations, *J. Geophys. Res.*, *112*, B08312, doi:10.1029/2007JB004983.

Wu, Y. M., L. Zhao, C. H. Chang, and Y. J. Hsu (2008), Focal mechanism determination in Taiwan by genetic algorithm, *Bull. Seismol. Soc. Am.*, *98*, 651–661, doi:10.1785/0120070115.

Yu, S. B., and L. C. Kuo (2001), Present-day crustal motion along the Longitudinal Valley Fault, eastern Taiwan, *Tectonophysics*, *333*, 199–217, doi:10.1016/S0040-1951(00)00275-4.

Yu, S. B., and L. C. Liu (1989), Fault creep on the central segment of the Longitudinal Valley Fault, eastern Taiwan, *Proc. Geol. Soc. China*, *32*, 209–231.

Yu, S. B., D. D. Jackson, G. K. Yu, and C. C. Liu (1990), Dislocation model for crustal deformation in the Longitudinal Valley area, eastern Taiwan, *Tectonophysics*, *183*, 97–109, doi:10.1016/0040-1951(90)90190-J.

Yu, S. B., H. Y. Chen, and L. C. Kuo (1997), Velocity field of GPS stations in the Taiwan area, *Tectonophysics*, *274*, 41–59, doi:10.1016/S0040-1951(96)00297-1.

Zebker, H. A., and J. Villasenor (1992), Decorrelation in interferometric radar surface echoes, *IEEE Trans. Geosci. Remote Sens.*, *30*(5), 950–959, doi:10.1109/36.175330.

Zebker, H. A., P. Rosen, and S. Hensley (1997), Atmospheric effects in interferometric synthetic aperture radar surface deformation and topographic maps, *J. Geophys. Res.*, *102*, 7547–7563, doi:10.1029/96JB03804.

R. Cattin, S. Dominguez, M. Leroy, M. Peyret, and A. Zajac, Géosciences Montpellier, Université Montpellier 2, CNRS UMR-5243, F-34095 Montpellier, France. (michel@gm.univ-montp2.fr)

J. Champenois, Laboratoire Géomatique, Télédétection, Modélisation des connaissances, Université Paris-Est, Boulevard Descartes, F-77454 Marne-la-Vallée, France.